

AIX-MARSEILLE UNIVERSITY  
DOCTORAL SCHOOL: Physics and Material Science  
PARTENAIRES DE RECHERCHE  
Laboratoire MADIREL

Submitted with the view of obtaining the degree of doctor

Discipline: Material Science  
Specialty: Characterisation of porous materials

Paul A. Iacomi

Titre de la thèse: sous-titre de la thèse

Defended on JJ/MM/AAAA in front of the following jury:

Prénom NOM	Affiliation	Rapporteur
Prénom NOM	Affiliation	Rapporteur
Prénom NOM	Affiliation	Examinateur
Prénom NOM	Affiliation	Examinateur
Prénom NOM	Affiliation	Examinateur
Prénom NOM	Affiliation	Directeur de thèse

National thesis number: 2017AIXM0001/001ED62



This work falls under the conditions of the [Creative Commons Attribution License - No commercial use - No modification 4.0 International](#).

# Abstract

Abstract is here.

# Acknowledgements

Acknowledgements go here

# Contents

<b>Abstract</b>	iii
<b>Acknowledgements</b>	iv
<b>1 Building a framework for adsorption data processing</b>	1
1.1 Introduction . . . . .	1
1.2 Methods implemented in pyGAPS . . . . .	1
1.2.1 Isotherm models . . . . .	1
1.2.2 Thickness functions . . . . .	7
1.2.3 BET surface area . . . . .	7
1.2.4 Langmuir surface area . . . . .	8
1.2.5 t-plot Method . . . . .	9
1.2.6 $\alpha_s$ Method . . . . .	9
1.2.7 Isosteric heat . . . . .	10
1.2.8 Kelvin model . . . . .	11
1.2.9 Mesoporous size distribution . . . . .	11
1.2.10 Microporous size distribution . . . . .	12
1.2.11 Multiscale size distribution - DFT fitting . . . . .	14
1.3 Method . . . . .	14
1.3.1 Intended use cases . . . . .	14
1.3.2 Core structure . . . . .	15
1.3.3 Creation of an Isotherm . . . . .	15
1.3.4 Workflow . . . . .	16
1.3.5 Units . . . . .	16
1.4 Case studies . . . . .	17
1.4.1 Routine characterization of a MOF sample . . . . .	17
1.4.2 Analysis of a carbon sample for gas separation applications . . . . .	20
1.5 Conclusion . . . . .	21
<b>2 Extending bulk analysis of porous compounds through calorimetry</b>	26
2.1 Introduction . . . . .	26
2.2 Literature . . . . .	26
2.3 Method . . . . .	26
2.4 Results and discussion . . . . .	26
2.5 Conclusion . . . . .	26
<b>3 Exploring the impact of synthesis and defects on adsorption measurements</b>	28
3.1 Introduction . . . . .	28
3.2 Literature . . . . .	28
3.3 Method . . . . .	28

## Contents

3.4 Results and discussion . . . . .	28
3.5 Conclusion . . . . .	28
<b>4 Exploring the impact of material form on adsorption measurements</b>	<b>30</b>
4.1 Introduction . . . . .	30
4.2 Shaping in context . . . . .	30
4.3 Synthesis, shaping and characterisation . . . . .	32
4.3.1 Material Synthesis . . . . .	32
4.3.2 Shaping Procedure . . . . .	33
4.3.3 Characterisation of powders and pellets . . . . .	33
4.3.4 Sample activation for adsorption . . . . .	33
4.4 Results and discussion . . . . .	33
4.4.1 Thermal stability . . . . .	33
4.4.2 Adsorption isotherms at 77K and room temperature . . . . .	35
4.4.3 Room temperature gas adsorption and microcalorimetry . . . . .	35
4.4.4 Vapour adsorption . . . . .	43
4.5 Conclusion . . . . .	45
<b>5 Exploring novel behaviours</b>	<b>51</b>
5.1 Introduction . . . . .	51
5.2 Literature . . . . .	51
5.3 Method . . . . .	51
5.4 Results and discussion . . . . .	51
5.5 Conclusion . . . . .	51
<b>Common characterisation techniques</b>	<b>53</b>
1 Thermogravimetry . . . . .	53
2 Bulk density determination . . . . .	53
3 Nitrogen physisorption at 77 K . . . . .	53
4 Gravimetric isotherms measured on Rubotherm Balance . . . . .	53
5 Vapour adsorption . . . . .	54
<b>Synthesis method of referenced materials</b>	<b>55</b>
1 UiO-66(Zr) for defect study . . . . .	55
2 UiO-66(Zr) for defect study . . . . .	55
3 UiO-66(Zr) for shaping study . . . . .	55
4 MIL-100(Fe) for shaping study . . . . .	55
5 MIL-127(Fe) for shaping study . . . . .	55
<b>Complete adsorption dataset for shaping study</b>	<b>56</b>
1 Calorimetry dataset UiO-66(Zr) . . . . .	56
2 Calorimetry MIL-100(Fe) . . . . .	57
3 Calorimetry MIL-127(Fe) . . . . .	60

# 1Building a framework for adsorption data processing

## 1.1 Introduction

Historically, the processing of isotherms was done by hand, with large worksheets being used for the calculations. As an example, we point out that one of the initial limitations of the BJH method was that each point had to be determined with an approximation of critical pore radius, due to the tedious work involved in the calculation.<sup>(1)</sup>

The advent of computers meant that the calculations could be performed quickly and reliably and led to the introduction of more complex methods for isotherm processing, such as the DFT method for pore size distribution.<sup>(2,3)</sup> Commercial adsorption equipment which offers the users a complete software solution for any isotherm calculations is now commonplace and makes obtaining reports of desired properties for measured materials a matter of minutes.

Given the current ubiquitousness of adsorption as a characterisation method, particularly for investigating surfaces and porous compounds, there is a large pool of data published in the scientific community. Key performance indicators such as specific surface area, working capacity and pore volume are commonly reported in scientific literature and used as benchmarking tools for comparing performance.

Recent efforts have also focused on building a database of adsorption isotherms,<sup>(4)</sup> to offer a searchable pool of standardised behaviours on different materials. This serves as both a useful reference for comparing synthesised compounds, as well as a method for quickly finding suitable materials which have the desired properties for a particular application.

In this work, we present pyGAPS, an open-source software package released under an MIT licence and written in Python, intended to be used for manipulation, storage, visualisation and processing of adsorption isotherms. Developed internally at the MADIREL Laboratory in Marseilles, the software is aimed to give users a powerful yet easy to use package that can perform the kind of processing usually offered by commercial software.

## 1.2 Methods implemented in pyGAPS

### 1.2.1 Isotherm models

#### The Henry model

Henry's law. Assumes a linear dependence of adsorbed amount with pressure.

Usually, Henry's law is unrealistic because the adsorption sites will saturate at higher pressures. Only use if your data is linear.

## BET model

The BET model assumes that adsorption happens on the surface of the material in incremental layers according to several assumptions:

- The adsorption sites are equivalent, and therefore the surface is heterogeneous
- There are no lateral interactions between adsorbed molecules
- The adsorption happens in layers, with adsorbed molecules acting as adsorption sites for new molecules
- The adsorption energy of a molecule on the second and higher layers equals the condensation energy of the adsorbent  $E_L$ .

A particular surface percentage  $\theta_x$  is occupied with  $x$  layers. For each layer at equilibrium, the adsorption and desorption rates must be equal. We can then apply the Langmuir theory for each layer.

$$k_{a_1}p\theta_0 = k_{d_1}\theta_1 \exp\left(-\frac{E_1}{RT}\right) \quad (1.1)$$

$$k_{a_2}p\theta_1 = k_{d_2}\theta_2 \exp\left(-\frac{E_L}{RT}\right) \quad (1.2)$$

$$\dots \quad (1.3)$$

$$k_{a_i}p\theta_{i-1} = k_{d_i}\theta_i \exp\left(-\frac{E_L}{RT}\right) \quad (1.4)$$

$$(1.5)$$

Since we are assuming that all layers beside the first have the same properties, we can define  $g = \frac{k_{d_2}}{k_{a_2}} = \frac{k_{d_3}}{k_{a_3}} = \dots$ . The coverages  $\theta$  can now be expressed in terms of  $\theta_0$ .

$$\theta_1 = y\theta_0 \quad \text{where} \quad y = \frac{k_{a_1}}{k_{d_1}}p \exp\left(-\frac{E_1}{RT}\right) \quad (1.6)$$

$$\theta_2 = x\theta_1 \quad \text{where} \quad x = \frac{p}{g} \exp\left(-\frac{E_L}{RT}\right) \quad (1.7)$$

$$\theta_3 = x\theta_2 = x^2\theta_1 \quad (1.8)$$

$$\dots \quad (1.9)$$

$$\theta_i = x^{i-1}\theta_1 = yx^{i-1}\theta_0 \quad (1.10)$$

$$(1.11)$$

A constant C may be defined such that

$$C = \frac{y}{x} = \frac{k_{a_1}}{k_{d_1}}g \exp\left(\frac{E_1 - E_L}{RT}\right)\theta_i = Cx^i\theta_0 \quad (1.12)$$

## 1 Building a framework for adsorption data processing

For all the layers, the equations can be summed:

$$\frac{n}{n_m} = \sum_{i=1}^{\infty} i\theta^i = C \sum_{i=1}^{\infty} ix^i\theta_0 \quad (1.13)$$

Since

$$\theta_0 = 1 - \sum_1^{\infty} \theta_i \sum_{i=1}^{\infty} ix^i = \frac{x}{(1-x)^2} \quad (1.14)$$

Then we obtain the BET equation

$$L(P) = \frac{n}{n_m} = M \frac{K_A P}{(1-K_B P)(1-K_B P + K_A P)} \quad (1.15)$$

### Langmuir and multi-site langmuir model

The Langmuir theory, proposed at the start of the 20th century, states that adsorption happens on active sites on a surface in a single layer. It is derived based on several assumptions.

- All sites are equivalent and have the same chance of being occupied
- Each adsorbate molecule can occupy one adsorption site
- There are no interactions between adsorbed molecules
- The rates of adsorption and desorption are proportional to the number of sites currently free and currently occupied, respectively
- Adsorption is complete when all sites are filled.

Using the following assumptions we can define rates for both the adsorption and desorption. The adsorption rate will be proportional to the number of sites available on the surface, as well as the number of molecules in the gas, which is represented by the pressure. The desorption rate, on the other hand, will be proportional to the number of occupied sites and the energy of adsorption. It is also useful to define  $\theta = \frac{n_a}{M}$  as the surface coverage, the number of sites occupied divided by the total sites. Mathematically:

$$v_a = k_a p (1 - \theta) v_d = k_d \theta \exp(-\frac{E}{RT}) \quad (1.16)$$

Here,  $M$  is the moles adsorbed at the completion of the monolayer, and therefore the maximum possible loading. At equilibrium, the rate of adsorption and the rate of desorption are equal, therefore the two equations can be combined.

$$k_a p (1 - \theta) = k_d \theta \exp(-\frac{E}{RT}) \quad (1.17)$$

Rearranging to get an expression for the loading, the Langmuir equation becomes:

$$L(P) = M \frac{KP}{1 + KP} \quad (1.18)$$

The Langmuir constant is the product of the individual desorption and adsorption constants  $k_a$  and  $k_d$  and exponentially related to the energy of adsorption  $\exp(-\frac{E}{RT})$ .

An extension to the Langmuir model is to consider the experimental isotherm to be the sum of several Langmuir-type isotherms with different monolayer capacities and affinities. The assumption is that the adsorbent presents several distinct types of homogeneous adsorption sites, and that separate Langmuir equations should be applied to each. This is particularly applicable in cases where the structure of the adsorbent suggests that different types of sites are present, such as in crystalline materials of variable chemistry like zeolites and MOFs. The resulting isotherm equation is:

$$L(P) = \sum_i M_i \frac{K_i P}{1 + K_i P} \quad (1.19)$$

In practice, up to three adsorption sites are considered. This model is the dual-site model ( $i = 2$ )

### Jensen Seaton model

When modelling adsorption in micropores, a requirement was highlighted by Jensen and Seaton in 1996<sup>(5)</sup> that at sufficiently high pressures the adsorption isotherm should not reach a horizontal plateau corresponding to saturation but that this asymptote should continue to rise due to the compression of the adsorbate in the pores. They came up with a semi-empirical equation to describe this phenomenon based on a function that interpolates between two asymptotes: the Henry's law asymptote at low pressure and an asymptote reflecting the compressibility of the adsorbate at high pressure.

Here  $K_H$  is the Henry constant,  $b$  is the compressibility of the adsorbed phase and  $c$  an empirical constant.

The equation can be used to model both absolute and excess adsorption as the pore volume can be incorporated into the definition of  $b$ , although this can lead to negative adsorption slopes for the compressibility asymptote. This equation has been found to provide a better fit for experimental data from microporous solids than the Langmuir or Toth equation, in particular for adsorbent/adsorbate systems with high Henry's constants where the amount adsorbed increases rapidly at relatively low pressures and then slows down dramatically.

### Quadratic model

The quadratic adsorption isotherm<sup>(6)</sup> exhibits an inflection point; the loading is convex at low pressures but changes concavity as it saturates, yielding an S-shape. The S-shape can be explained by adsorbate-adsorbate attractive forces; the initial convexity is due

to a cooperative effect of adsorbate-adsorbate attractions aiding in the recruitment of additional adsorbate molecules.

The parameter  $K_a$  can be interpreted as the Langmuir constant; the strength of the adsorbate-adsorbate attractive forces is embedded in  $K_b$ .

### Temkin model

The Temkin adsorption isotherm,<sup>(7)</sup> like the Langmuir model, considers a surface with M identical adsorption sites, but takes into account adsorbate- adsorbate interactions by assuming that the heat of adsorption is a linear function of the coverage. The Temkin isotherm is derived using a mean-field argument and used an asymptotic approximation to obtain an explicit equation for the loading.<sup>(8)</sup>

Here, M and K have the same physical meaning as in the Langmuir model. The additional parameter  $\theta$  describes the strength of the adsorbate-adsorbate interactions ( $\theta < 0$  for attractions).

### Toth model

The Toth model is an empirical modification to the Langmuir equation. The parameter  $t$  is a measure of the system heterogeneity.

Thanks to this addition parameter, the Toth equation can accurately describe a large number of adsorbent/adsorbate systems and is recommended as the first choice of isotherm equation for fitting isotherms of many adsorbents such as hydrocarbons, carbon oxides, hydrogen sulphide and alcohols on activated carbons but also zeolites.

### Virial model

A virial isotherm model attempts to fit the measured data to a factorized exponent relationship between loading and pressure.<sup>(9)</sup>

$$P = n \exp(K_1 n^0 + K_2 n^1 + K_3 n^2 + K_4 n^3 + \dots + K_i n^{i-1}) \quad (1.20)$$

It has been applied with success to describe the behaviour of standard as well as supercritical isotherms. The factors are usually empirical, although some relationship with physical can be determined: the first constant is related to the Henry constant at zero loading, while the second constant is a measure of the interaction strength with the surface.

$$K_1 = -\ln K_{H,0} \quad (1.21)$$

In practice, besides the first constant, only 2-3 factors are used.

### Vacancy solution theory models

As a part of the Vacancy Solution Theory (VST) family of models, it is based on concept of a “vacancy” species, denoted v, and assumes that the system consists of a mixture of these vacancies and the adsorbate.

## 1 Building a framework for adsorption data processing

The VST model is defined as follows:

- A vacancy is an imaginary entity defined as a vacuum space which acts as the solvent in both the gas and adsorbed phases.
- The properties of the adsorbed phase are defined as excess properties in relation to a dividing surface.
- The entire system including the adsorbent are in thermal equilibrium however only the gas and adsorbed phases are in thermodynamic equilibrium.
- The equilibrium of the system is maintained by the spreading pressure which arises from a potential field at the surface

It is possible to derive expressions for the vacancy chemical potential in both the adsorbed phase and the gas phase, which when equated give the following equation of state for the adsorbed phase:

$$\pi = -\frac{R_g T}{\sigma_v} \ln y_v x_v \quad (1.22)$$

where  $y_v$  is the activity coefficient and  $x_v$  is the mole fraction of the vacancy in the adsorbed phase. This can then be introduced into the Gibbs equation to give a general isotherm equation for the Vacancy Solution Theory where  $K_H$  is the Henry's constant and  $f(\theta)$  is a function that describes the non-ideality of the system based on activity coefficients:

$$P = \frac{n_{ads}}{K_H} \frac{\theta}{1-\theta} f(\theta) \quad (1.23)$$

The general VST equation requires an expression for the activity coefficients. The Wilson<sup>(10)</sup> equation can be used, which expresses the activity coefficient in terms of the mole fractions of the two species (adsorbate and vacancy) and two constants  $\Lambda_{1v}$  and  $\Lambda_{v1}$ . The equation becomes:

$$P = \left( \frac{n_{ads}}{K_H} \frac{\theta}{1-\theta} \right) \left( \Lambda_{1v} \frac{1 - (1 - \Lambda_{v1})\theta}{\Lambda_{1v} + (1 - \Lambda_{v1})\theta} \right) \exp \left( - \frac{\Lambda_{v1}(1 - \Lambda_{v1})\theta}{1 - (1 - \Lambda_{v1})\theta} - \frac{(1 - \Lambda_{1v})\theta}{\Lambda_{1v} + (1 - \Lambda_{1v})\theta} \right) \quad (1.24)$$

Cochran<sup>(11)</sup> developed a simpler, three parameter equation based on the Flory–Huggins equation for the activity coefficient. The equation for then becomes:

$$P = \left( \frac{n_{ads}}{K_H} \frac{\theta}{1-\theta} \right) \exp \frac{\alpha_{1v}^2 \theta}{1 + \alpha_{1v} \theta} \alpha_{1v} = \frac{\alpha_1}{\alpha_v} - 1 \quad (1.25)$$

where  $\alpha_1$  and  $\alpha_v$  are the molar areas of the adsorbate and the vacancy respectively.

## 1.2.2 Thickness functions

### 1.2.3 BET surface area

The BET surface area is one of the first standardised methods to calculate the surface area of a porous material.<sup>(12)</sup> It is generally applied on isotherms obtained through N2 adsorption at 77K, although other adsorbates (Ar, Kr) have been used.

It assumes that the adsorption happens on the surface of the material in incremental layers according to the BET theory. Even if the adsorbent is porous, the initial amount adsorbed (usually between 0.05 - 0.4  $p/p_0$ ) can be modelled through the BET equation:

$$\frac{p/p_0}{n_{ads}(1-p/p_0)} = \frac{1}{n_m C} + \frac{C-1}{n_m C} (p/p_0) \quad (1.26)$$

Therefore, if we plot the isotherm points as  $\frac{p/p_0}{n_{ads}(1-p/p_0)}$  versus  $p/p_0$ , a linear region can usually be found. The slope and intercept of this line can then be used to calculate  $n_m$ , the amount adsorbed at the statistical monolayer, as well as C, the BET constant.

$$n_m = \frac{1}{s+i} C = \frac{s}{i} + 1 \quad (1.27)$$

The surface area can then be calculated by using the moles adsorbed at the statistical monolayer. If the specific area taken by one of the adsorbate molecules on the surface is known, it is inserted in the following equation together with Avogadro's number:

$$a(BET) = n_m A_N \sigma \quad (1.28)$$

#### *Limitations*

While a standard for surface area determinations, the BET area should be used with care, as there are many assumptions made in the calculation. To augment the validity of the BET method, Rouquerol<sup>(13)</sup> proposed several checks to ensure that the BET region selected is valid:

- The BET constant (C) obtained should be positive
- In the corresponding Rouquerol plot where  $n_{ads}(1-p/p_0)$  is plotted with respect to  $p/p_0$ , the points chosen for BET analysis should be strictly increasing
- The loading at the statistical monolayer should be situated within the limits of the BET region

This module implements all these checks.

Regardless, the BET surface area should still be interpreted carefully. The following assumptions are implicitly made in this approach:

- Adsorption takes place on the pore surface. Microporous materials which have pores in similar size as the molecule adsorbed cannot have a realistic surface area

- The cross-sectional area of the molecule on the surface cannot be guaranteed. For example, nitrogen has been known to adopt a different conformation on the surface of some materials, due to inter-molecular forces, which effectively lowers its cross-sectional area.
- No account is made for adsorbate-adsorbent interaction in BET theory

### 1.2.4 Langmuir surface area

The Langmuir theory,<sup>(14)</sup> proposed at the start of the 20th century, states that adsorption happens on active sites on a surface in a single layer. It is derived based on several assumptions.

- All sites are equivalent and have the same chance of being occupied
- Each adsorbate molecule can occupy one adsorption site
- There are no interactions between adsorbed molecules
- The rates of adsorption and desorption are proportional to the number of sites currently free and currently occupied, respectively
- Adsorption is complete when all sites are filled.

The Langmuir equation is then:

$$n = n_m \frac{KP}{1 + KP} \quad (1.29)$$

The equation can be rearranged as:

$$\frac{P}{n} = \frac{1}{Kn_m} + \frac{P}{n_m} \quad (1.30)$$

Assuming the data can be fitted with a Langmuir model, by plotting  $\frac{P}{n}$  against pressure, a line will be obtained. The slope and intercept of this line can then be used to calculate  $n_m$ , the amount adsorbed at the monolayer, as well as K, the Langmuir constant.

$$n_m = \frac{1}{s} K = \frac{1}{i * n_m} \quad (1.31)$$

The surface area can then be calculated by using the moles adsorbed at the monolayer. If the specific area taken by one of the adsorbate molecules on the surface is known, it is inserted in the following equation together with Avogadro's number:

$$a(\text{Langmuir}) = n_m A_N \sigma \quad (1.32)$$

Limitations

The Langmuir method for determining surface area assumes that only one single layer is adsorbed on the surface of the material. As most adsorption processes (except chemisorption) don't follow this behaviour, it is important to regard the Langmuir surface area as an estimate.

### 1.2.5 t-plot Method

The t-plot method attempts to relate the adsorption on a material with an ideal curve which describes the thickness of the adsorbed layer on a surface.<sup>(15)</sup> A plot is constructed, with the isotherm loading data plotted versus thickness values obtained through the model. It stands to reason that, in the case that the experimental adsorption curve follows the model, a straight line will be obtained with its intercept through the origin. However, since in most cases there are differences between adsorption in the pores and ideal surface adsorption, the t-plot will deviate and form features which can be analysed to describe the material characteristics.

- a sharp vertical deviation will indicate condensation in a type of pore
- a gradual slope will indicate adsorption on the wall of a particular pore

The slope of the linear section can be used to calculate the area where the adsorption is taking place. If it is of a linear region at the start of the curve, it will represent the total surface area of the material. If at the end of the curve, it will instead represent external surface area of the sample. The formula to calculate the area is where  $\rho_l$  is the liquid density of the adsorbate at experimental conditions

$$A = \frac{sM_m}{\rho_l} \quad (1.33)$$

If the region selected is after a vertical deviation, the intercept of the line will no longer pass through the origin. This intercept be used to calculate the pore volume through the following equation:

$$V_{ads} = \frac{iM_m}{\rho_l} \quad (1.34)$$

Since the t-plot method is taking the differences between the isotherm and a model, care must be taken to ensure that the model actually describes the thickness of a layer of adsorbate on the surface of the adsorbent. This is more difficult than it appears as no universal thickness curve exists. When selecting a thickness model, make sure that it is applicable to both the material and the adsorbate. Interactions at loadings that occur on the t-plot lower than the monolayer thickness do not have any physical meaning.

### 1.2.6 $\alpha_s$ Method

In order to extend the t-plot analysis with other adsorbents and non-standard thickness curves, the  $\alpha_s$  method was devised.<sup>(16)</sup> Instead of a formula that describes the thickness

of the adsorbed layer, a reference isotherm is used. This isotherm is measured on a non-porous version of the material with the same surface characteristics and with the same adsorbate. The  $\alpha_s$  values are obtained from this isotherm by regularisation with an adsorption amount at a specific relative pressure, usually taken as 0.4 since nitrogen hysteresis loops theoretically close at this value.

$$\alpha_s = \frac{n_a}{n_{0.4}} \quad (1.35)$$

The analysis then proceeds as in the t-plot method.

The slope of the linear section can be used to calculate the area where the adsorption is taking place. If it is of a linear region at the start of the curve, it will represent the total surface area of the material. If at the end of the curve, it will instead represent external surface area of the sample. The calculation uses the known area of the reference material. If unknown, the area will be calculated here using the BET method.

$$A = \frac{sA_{ref}}{(n_{ref})_{0.4}} \quad (1.36)$$

If the region selected is after a vertical deviation, the intercept of the line will no longer pass through the origin. This intercept be used to calculate the pore volume through the following equation:

$$V_{ads} = \frac{iM_m}{\rho_l} \quad (1.37)$$

The reference isotherm chosen for the  $\alpha_s$  method must be a description of the adsorption on a completely non-porous sample of the same material. It is often impossible to obtain such non-porous versions, therefore care must be taken how the reference isotherm is defined.

### 1.2.7 Isosteric heat

The isosteric heats are calculated from experimental data using the Clausius-Clapeyron equation as the starting point:

$$\left( \frac{\partial \ln P}{\partial T} \right)_{n_a} = -\frac{\Delta H_{ads}}{RT^2} \quad (1.38)$$

Where  $\Delta H_{ads}$  is the enthalpy of adsorption. In order to approximate the partial differential, two or more isotherms are measured at different temperatures. The assumption made is that the heat of adsorption does not vary in the temperature range chosen. Therefore, the isosteric heat of adsorption can be calculated by using the pressures at which the loading is identical using the following equation for each point:

$$\Delta H_{ads} = -R \frac{\partial \ln P}{\partial 1/T} \quad (1.39)$$

and plotting the values of  $\ln P$  against  $1/T$  we should obtain a straight line with a slope of  $-\Delta H_{ads}/R$ .

### \*Limitations\*

The isosteric heat is sensitive to the differences in pressure between the two isotherms. If the isotherms measured are too close together, the error margin will increase.

The method also assumes that enthalpy of adsorption does not vary with temperature. If the variation is large for the system in question, the isosteric heat calculation will give unrealistic values.

Even with carefully measured experimental data, there are two assumptions used in deriving the Clausius-Clapeyron equation: an ideal bulk gas phase and a negligible adsorbed phase molar volume. These have a significant effect on the calculated isosteric heats of adsorption, especially at high relative pressures and for heavy adsorbates.

### 1.2.8 Kelvin model

The standard kelvin equation for determining critical pore radius for condensation or evaporation.

### \*Limitations\*

The Kelvin equation assumes that adsorption in a pore is not different than adsorption on a standard surface. Therefore, no interactions with the adsorbent is accounted for.

Furthermore, the geometry of the pore itself is considered to be invariant accross the entire adsorbate.

Calculates the pore size distribution using a 'classical' model which attempts to describe the adsorption in a pore as a combination of a statistical thickness and a condensation/evaporation behaviour described by surface tension

Currently, the methods provided are:

- the BJH or Barrett, Joyner and Halenda method - the DH or Dollimore-Heal method, an extension of the BJH method

A common mantra of data processing is: "garbage in = garbage out". Only use methods when you are aware of their limitations and shortcomings.

According to Rouquerol, in adopting this approach, it is assumed that:

- The Kelvin equation is applicable over the pore range (mesopores). Therefore in pores which are below a certain size (around 2.5 nm), the granularity of the liquid-vapour interface becomes too large for classical bulk methods to be applied.
- The meniscus curvature is controlled be the pore size and shape. Ideal shapes for the curvature are assumed.
- The pores are rigid and of well defined shape. They are considered open-ended and non-intersecting
- The filling/emptying of each pore does not depend on its location.
- The adsorption on the pore walls is not different from surface adsorption.

### 1.2.9 Mesoporous size distribution

The BJH or Barrett, Joyner and Halenda method for calculation of pore size distribution is based on a classical description of the adsorbate behaviour in the adsorbent pores.<sup>(1)</sup> Under this method, the adsorbate is adsorbing on the pore walls in a predictable way,

and decreasing the apparent pore volume until condensation takes place, filling the entire pore. The two variables, layer thickness and radius where condensation takes place can be modelled by a thickness model (such as Halsey, Harkins & Jura, etc.) and a critical radius model for condensation/evaporation, based on a form of the Kelvin equation.

$$r_p = t + r_k \quad (1.40)$$

The original model used the desorption curve as a basis for calculating pore size distribution. Between two points of the curve, the volume desorbed can be described as the volume contribution from pore evaporation and the volume from layer thickness decrease as per the equation above. The computation is done cumulatively, starting from the filled pores and calculating for each point the volume adsorbed in a pore from the following equation:

$$V_p = \left( \frac{\bar{r}_p}{\bar{r}_k + \Delta t_n} \right)^2 \quad (1.41)$$

$$(\Delta V_n - \Delta t_n \sum_{i=1}^{n-1} \Delta A_p) \quad (1.42)$$

$$+ \Delta t_n \bar{t}_n \sum_{i=1}^{n-1} \frac{\Delta A_p}{\bar{r}_p} )A = 2\Delta V_p / r_p \quad (1.43)$$

Where:

- $\Delta A_p$  is the area of the pores
- $\Delta V_p$  is the adsorbed volume change between two points
- $\bar{r}_p$  is the average pore radius calculated as a sum of the kelvin radius and layer thickness of the pores at pressure p between two measurement points
- $\bar{r}_k$  is the average kelvin radius between two measurement points
- $\bar{t}_n$  is the average layer thickness between two measurement points
- $\Delta t_n$  is the average change in layer thickness between two measurement points

Then, by plotting  $\Delta V / (2 * \Delta r_p)$  versus the width of the pores calculated for each point, the pore size distribution can be obtained.

### 1.2.10 Microporous size distribution

The H-K method attempts to describe the adsorption within pores by calculation of the average potential energy for a pore.<sup>(17)</sup> The method starts by assuming the relationship between the gas phase as being:

$$R_g T \ln\left(\frac{p}{p_0}\right) = U_0 + P_a \quad (1.44)$$

Here  $U_0$  is the potential function describing the surface to adsorbent interactions and  $P_a$  is the potential function describing the adsorbate- adsorbate interactions. This equation is derived from the equation of the free energy of adsorption at constant temperature where term  $T\Delta S^{tr}(w/w_\infty)$  is assumed to be negligible.

If a Lennard-Jones-type potential function describes the interactions between the adsorbate molecules and the adsorbent molecules then the two contributions to the total potential can be replaced by the extended function. The resulting equation becomes:

$$RT \ln(p/p_0) = N_A \frac{n_a A_a + n_A A_A}{2\sigma^4(l-d)} \quad (1.45)$$

$$\times \int_{d/2}^{1-d/2} \left[ -\left(\frac{\sigma}{r}\right)^4 + \left(\frac{\sigma}{r}\right)^{10} - \left(\frac{\sigma}{l-r}\right)^4 + \left(\frac{\sigma}{l-r}\right)^{10} \right] dx \quad (1.46)$$

Where:

- $R$  – gas constant
- $T$  – temperature
- $l$  – width of pore
- $d$  – defined as  $d = d_a + d_A$  the sum of the diameters of the adsorbate and adsorbent molecules
- $N_A$  – Avogadro's number
- $n_a$  – number of molecules of adsorbent
- $A_a$  – the Lennard-Jones potential constant of the adsorbent molecule defined as

$$A_a = \frac{6mc^2\alpha_a\alpha_A}{\alpha_a/\varkappa_a + \alpha_A/\varkappa_A} \quad (1.47)$$

- $A_A$  – the Lennard-Jones potential constant of the adsorbate molecule defined as

$$A_a = \frac{3mc^2\alpha_A\varkappa_A}{2} \quad (1.48)$$

- $m$  – mass of an electron
- $c$  – speed of light in vacuum
- $\alpha_a$  – polarizability of the adsorbate molecule

- $\alpha_A$  – polarizability of the adsorbent molecule
- $\varkappa_a$  – magnetic susceptibility of the adsorbate molecule
- $\varkappa_A$  – magnetic susceptibility of the adsorbent molecule

\*Limitations\*

The assumptions made by using the H-K method are:

- It does not have a description of capillary condensation. This means that the pore size distribution can only be considered accurate up to a maximum of 5 nm.
- Each pore is uniform and of infinite length. Materials with varying pore shapes or highly interconnected networks may not give realistic results.
- The wall is made up of single layer atoms. Furthermore, since the HK method is reliant on knowing the properties of the surface atoms as well as the adsorbent molecules the material should ideally be homogenous.
- Only dispersive forces are accounted for. If the adsorbate-adsorbent interactions have other contributions, the Lennard-Jones potential function will not be an accurate description of pore environment.

### 1.2.11 Multiscale size distribution - DFT fitting

The function will take the data in the form of pressure and loading. It will then load the kernel either from disk or from memory and define a minimization function as the sum of squared differences of the sum of all individual kernel isotherm loadings multiplied by their contribution as per the following function:

$$f(x) = \sum_{p=p_0}^{p=p_x} (n_{p,exp} - \sum_{w=w_0}^{w=w_y} n_{p,kernel} X_w)^2 \quad (1.49)$$

## 1.3 Method

### 1.3.1 Intended use cases

The software was imagined for use in two types of scenario. First, as a command line interface, in environments such as IPython and Jupyter. The typical user working in these environments is likely to be processing a small batch of results at one time, and is interested in obtaining the results in graphical form. For this type of application, the framework should provide an unobtrusive way of importing the user data, as well as present an API which does not require extensive knowledge of processing methods. Finally, a powerful graphing environment is required which will allow the user to visualise their original dataset and results.

The second envisaged application is related to bulk data processing. Requirements here shift towards parameter control, scripting and extensibility. The framework API should offer the option to change implicit parameters, select calculation limits and return the results in a numerical form for further processing. This type of application is also likely to require storage of isotherms in a database or under other types of data files.

### 1.3.2 Core structure

In order to offer a clear structuring of functionality, pyGAPS introduces several classes which abstract data and functionality for facile interaction. The classes are intuitively named: `Isotherm`, `Sample` and `Adsorbent`.

The `Isotherm` class is a representation of an adsorption isotherm i.e. a function of the amount adsorbed, or loading, with pressure at a fixed temperature. The class also contains other information relating to the isotherm, such as the material name and batch it describes, the adsorbate used and other user-defined properties.

Because the aforementioned relationship can be either a physical measurement defined by individual pressure-loading pairs or a model, describing the relationship as a function rather than discrete data, the `Isotherm` class is used as a parent class for two subclasses: `PointIsotherm`, describing datapoints and `ModelIsotherm` containing a model such as Henry, Langmuir etc., which encapsulate the respective functionality. The two classes are interchangeable as they share most methods and properties. Once an instance of an `Isotherm` class is created, it can then be used for the processing, conversion and graphing capabilities of pyGAPS.

The isotherm classes contain the name and batch of the sample they are measured on in a string format. The user might want to specify other information about the material, such as the date of synthesis or the material's density, as well as store this information in the database. For this case, pyGAPS provides the `Sample` class. The framework uses the string values in the isotherm to connect an `Isotherm` instance to a specific `Sample`.

Finally, in order for many of the calculations included in pyGAPS to be performed, properties of the adsorbate used are needed e.g. liquid density, vapour pressure etc. The `Adsorbate` class is provided for this purpose, which is connected to an `Isotherm` class similarly to a `Sample`. The physical properties are either calculated in the background through an equation of state, either the open source CoolProp library<sup>(18)</sup> or the NIST-made REFPROP.<sup>(19)</sup> The properties can also be retrieved from the internal database or specified by the user.

### 1.3.3 Creation of an Isotherm

An `Isotherm` can be created either from the command line directly or through an import from a supported format. For the direct creation, the code takes two kinds of inputs: the data itself, in the form of a `pandas.DataFrame`, and the isotherm parameters describing it. Only four parameters are strictly required: the material name, the material batch, the adsorbate used and the experimental temperature. Other parameters can be passed as well and will be stored in the isotherm class.

The `DataFrame` must contain a column containing the pressure points and one containing the corresponding loading points of the isotherm. Other columns can also be passed, when secondary data such as enthalpy of adsorption is present at each measurement point. These columns will be saved in the case of the `PointIsotherm` class and can be plotted afterwards.

If no unit data is specified in the constructor, the framework will assume that the isotherm is in units of  $\text{mmol g}^{-1}$  loading as a function of bar. Both the units and the basis can be specified, as it is explained in a latter section.

Finally, the data is saved in the newly created class or used to generate parameters for a model such as BET, Langmuir, etc., in the case of a `PointIsotherm` and `ModelIsotherm` respectively. It should be noted that the creation of `Sample` and `Adsorbate` instances is similar.

Alternatively, the isotherm can be imported from a file containing a format that is recognised by `pyGAPS`. Parsing from suitably structured JSON, CSV and Excel files is supported.

### 1.3.4 Workflow

Once an isotherm object is created, it will be used for all further processing. The class contains methods which can be used to inspect the data visually, or retrieve parts of the isotherm such as the adsorption or desorption branches with user-chosen limits or units. Singular values of pressure or loading can be calculated, either through interpolation in the case of a `PointIsotherm` or by evaluation of the internal model in the `ModelIsotherm`. For an isotherm with datapoints, these can also be converted into different units or modes.

Characterisation functions take a single isotherm object as their first parameter. This is the case for the BET area, Langmuir area, t-plot,  $\alpha_s$  plot, and pore size distribution methods. These characterisation functions attempt to automate as much of the process as possible. For example, the BET area limits are automatically calculated using the Rouquerol<sup>(13)</sup> method, with all the checks implemented into the code. In another example the straight line sections of the t-plot are determined automatically through a calculation of the second derivative of the transformed isotherm. For detailed control, there is an option to specify options for each individual method, such as manual BET limits, different thickness functions for the t-plot or Kelvin-based mesoporous pore distribution methods, custom parameters for the Horvath-Kawazoe microporous pore distribution, custom DFT or NLDFT kernels and more. The results are returned in a dictionary or can be directly graphed if the `verbose` parameter is passed.

### 1.3.5 Units

When computers work with physical data, units are often a matter that introduces confusion. Here we explain how `pyGAPS` handles units and other physical world concepts such as relative pressure and mass or volume basis.

The following dimensions can be specified for an Isotherm: the measurement *pressure*, the quantity of guest adsorbed or *loading* and the amount of adsorbent material the loading is reported on, or *adsorbent*.

Pressure can be reported either in an absolute value, in several common units such as bar, torr, Pa, or as *relative pressure*, the pressure divided by the saturation vapour pressure of the adsorbate at the respective measurement temperature. Conversions between the two modes are automatic and handled internally.

Both the *loading* and *adsorbent* can be reported in three different bases: a molar basis, a mass basis or a volume basis. Within each basis different units are recognised and can be easily converted. The conversions between bases can also easily performed if the required conversion factors (i.e. molar mass and density) are available. For *loading*, these factors are automatically calculated internally, while for the *adsorbent* they should be provided by the user in the respective `Sample` class.

## 1.4 Case studies

### 1.4.1 Routine characterization of a MOF sample

The UiO-66(Zr) MOF and its derivatives are well known due to their thermal and chemical stability.<sup>(20)</sup> It is composed of  $[\text{Zr}_6\text{O}_4(\text{OH})_4]^{12+}$  clusters which are connected with benzene dicarboxilate (BDC) linkers to form a face-centered cubic framework. It has shown promise<sup>(21)</sup> in use for gas adsorption and catalytic applications.

When a newly synthesised sample is available, an initial characterisation is often performed to compare the material with previous batches. Adsorption of nitrogen at 77 K is commonly used to verify if predictors such as specific surface area and pore size distribution are consistent with other samples or literature values.

The nitrogen isotherm is first imported in pyGAPS. To obtain the BET area, the `pygaps.area_BET()` method is used with the isotherm object as the parameter and the verbose option, with Figure 1.1 as the output. It can be seen that the framework has automatically selected the points within the applicable BET region using the checks devised by Rouquerol et al.<sup>(13)</sup> to assert method validity. The statistical BET monolayer point is within the selected region, which is one of the checks implemented for method validity. The calculated surface area is 1277 m<sup>2</sup>/g, which is similar to literature values.<sup>(21,22)</sup>

The same isotherm is used to calculate the pore size distribution of the UiO-66(Zr) sample. This MOF has octahedral cages surrounded by eight corner tetrahedral cages of 11 and 8 Å respectively. The structure is therefore expected to have only micropores. Two methods are available in pyGAPS for micropore size distributions: a ‘classical’ Horvath-Kawazoe (HK) method,<sup>(17)</sup> as well as a DFT fitting routine. The HK method is called by using the function in Listing 1.1. Here, the surface characteristic parameters determined by Saito and Foley<sup>(23)</sup> are to be used, with the framework automatically supplying the parameters for the adsorbed gas.

Listing 1.1: Calculating the PSD

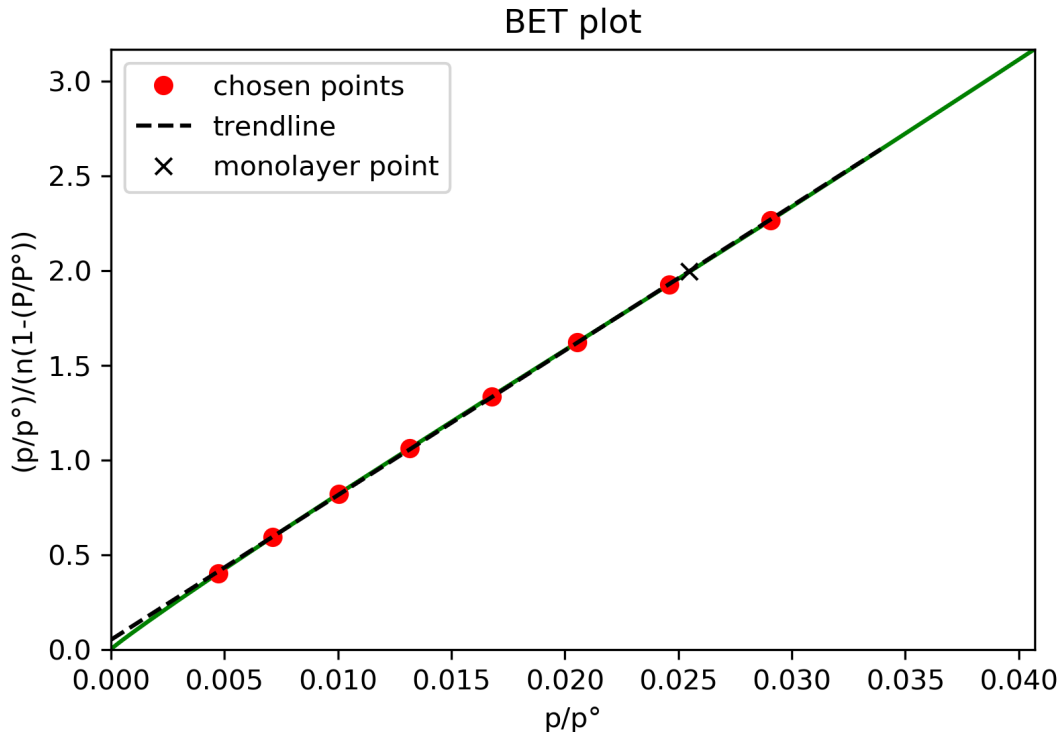


Figure 1.1: BET transformation and point selection

```
pygaps.micropore_size_distribution(iso,
                                    psd_model='HK',
                                    adsorbent_model='OxideIon(SF)')
pygaps.dft_size_distribution(iso, kernel_path='internal')
```

The DFT fitting is done using the internal kernel which is applicable for N<sub>2</sub> on carbon slit pores and included with pyGAPS. Results are shown in Figure 1.2. We can see that whilst both methods produce a bimodal size distribution, neither is accurate in describing the crystallographic pore widths. This is to be expected, since neither method is applicable to the UiO-66(Zr) system. However, when comparing two samples of the same MOF, these methods can still highlight differences in the quality of the two batches. For example, it can be seen that the DFT method shows wide peaks at >1 nm which can be an indication of the presence of defects in the UiO-66(Zr) structure. Indeed, TGA analysis of the pristine sample shows a linker ratio (11.8 linkers per cluster) that is lower than it would be in a perfect sample (see figure in supplemental information.)

New materials are often screened for their ability to act as a CO<sub>2</sub> capture material. A good predictor of performance in this application are the enthalpies of adsorption, which are an indication of host-guest interactions. Here, we first measure the differential heats of adsorption directly through the use of adsorption microcalorimetry at 303 K. Then, to determine the isosteric heats of adsorption, two isotherms have been measured at 303 K and 323 K respectively. The complete set of isotherms is loaded into pyGAPS and

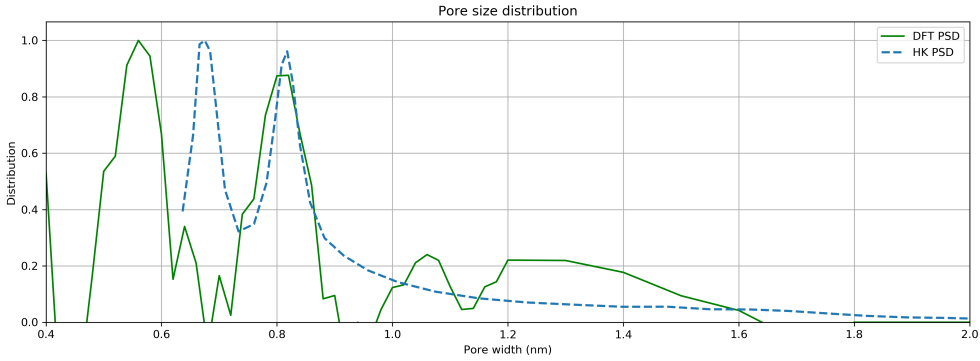


Figure 1.2: Pore size distribution calculated through the Horvath-Kawazoe method (dotted blue line) and the internal DFT kernel (continuous green line)

plotted by the `pygaps.plot_iso()` function as seen in Figure 1.3a. To calculate the isosteric heat of adsorption, the two isotherms measured for this purpose are passed through the `pygaps.isosteric_heat()` function. The results from the calculation are overlaid on top of the measured calorimetric data in Figure 1.3b. The two datasets are overlap for the most part but diverge at low loadings and near complete coverage. At low loading the small changes in pressure amount introduce large errors in the Clausius-Clapeyron equation. This, together with the breakdown of the assumption of equilibrium due to active sites in the MOF lead to the calorimetric measurement providing more valid results. At higher loadings, where the isotherm reaches a plateau and the change in adsorbed amount is small from point to point, errors are introduced in the direct calculation of the heat of adsorption. The two techniques are thus complementary.

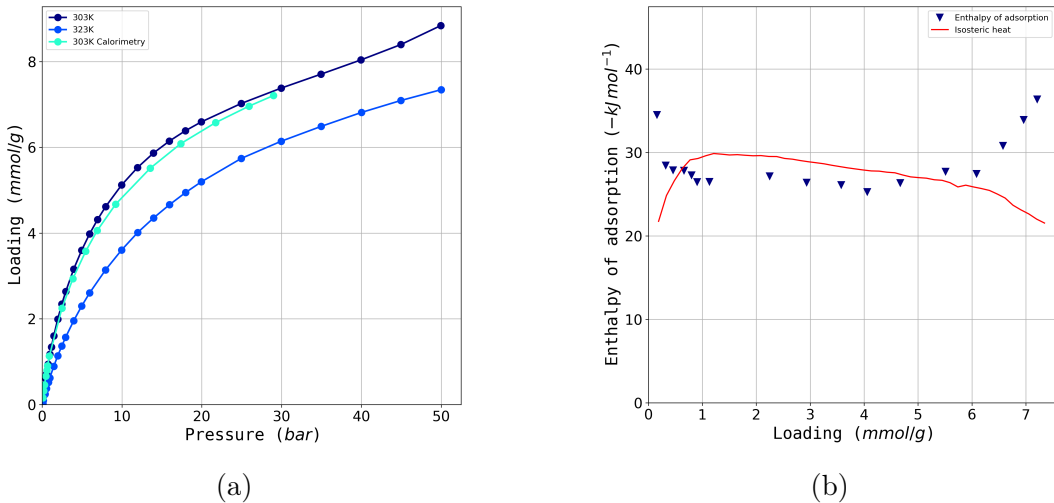


Figure 1.3: Calculation of enthalpy of adsorption: (a) the dataset of isotherms used and (b) the calculated isosteric heat (red line) together with the measured differential enthalpy of adsorption (blue triangles)

## 1.4.2 Analysis of a carbon sample for gas separation applications

A sample of reference carbon Takeda 5A is to be investigated for an in-depth characterisation of the adsorption behaviour of pure gases, with a focus on describing the pore environment. Afterwards, the performance of different binary separations is evaluated, such as CO<sub>2</sub>/N<sub>2</sub> and propane/propylene.

Pure gas adsorption data has been recorded at 303 K in conjunction with microcalorimetry on N<sub>2</sub>, CO, CO<sub>2</sub>, CH<sub>4</sub>, C<sub>2</sub>H<sub>6</sub>, C<sub>3</sub>H<sub>6</sub> and C<sub>3</sub>H<sub>8</sub>. The complete dataset is plotted with the pygaps.plot\_iso() function and can be seen in Figure 1.4a.

Nitrogen and carbon monoxide are similar in their adsorption behaviour, with a nearly linear isotherm and low capacities. Hydrocarbons are adsorbed with higher loadings, with both propane and propylene reaching a plateau at low pressures. Propylene is seen to have a higher capacity than propane, with packing effects as a likely cause. Carbon dioxide has the highest loading capacity of the entire dataset.

Two parameters can be useful in characterising the local pore environment before guest-guest interactions come into effect: the Henry constant at low loadings as well as the initial enthalpy of adsorption. Both can be calculated with pyGAPS, with several options in regard to the methodology. Here, Henry's constant is calculated using the pygaps.initial\_henry\_virial() function, which fits a virial model to the isotherm and then takes the limit at loading approaching zero. The initial enthalpy of adsorption is obtained through the pygaps.initial\_enthalpy\_comp() function. This fits the enthalpy curve to a compound contribution from guest-host interaction, defects, guest-guest attraction and repulsion using a minimization algorithm. The results of the calculations are plotted versus the polarizability of the gas used, which can be obtained from the respective `Adsorbate` class. Figure 1.4b shows that both the parameters fall on a linear trend, which suggests that the interactions between those guests and the pore walls are mostly due to Lennard-Jones interactions. Carbon dioxide has a higher enthalpy of adsorption than the baseline due to the contribution from its quadrupole moment. There is almost a complete overlap between propane and propylene, which leads to the conclusion that the unsaturated double bond does not interact in a specific way with the carbon surface. The difference between the two isotherms is due exclusively to steric and packing effects.

From the analysis of the pure gas dataset and the property-polarizability graph, two potentially interesting separations arise, namely CO<sub>2</sub>-N<sub>2</sub> and propylene-propane. For these two pairs we use ideal adsorbed solution theory (IAST) to simulate binary adsorption behaviour. The pyGAPS framework includes a modified version of the pyIAST code<sup>(24)</sup> which has been adapted to work with the `Isotherm` classes. Both model isotherms and real data can be used for IAST, with spreading pressure being calculated through the underlying isotherm model or through interpolation, respectively. Based on the previous analysis, we expect to see good performance for carbon dioxide capture and little or no selectivity in the paraffin-olefin pair.

In this case, we fit the experimental data to the available models in pyGAPS, then use the resulting model isotherms for IAST simulations. In order to get a 'best-fit' model isotherm, we use the function in Listing 1.2, which fits all available models and selects the

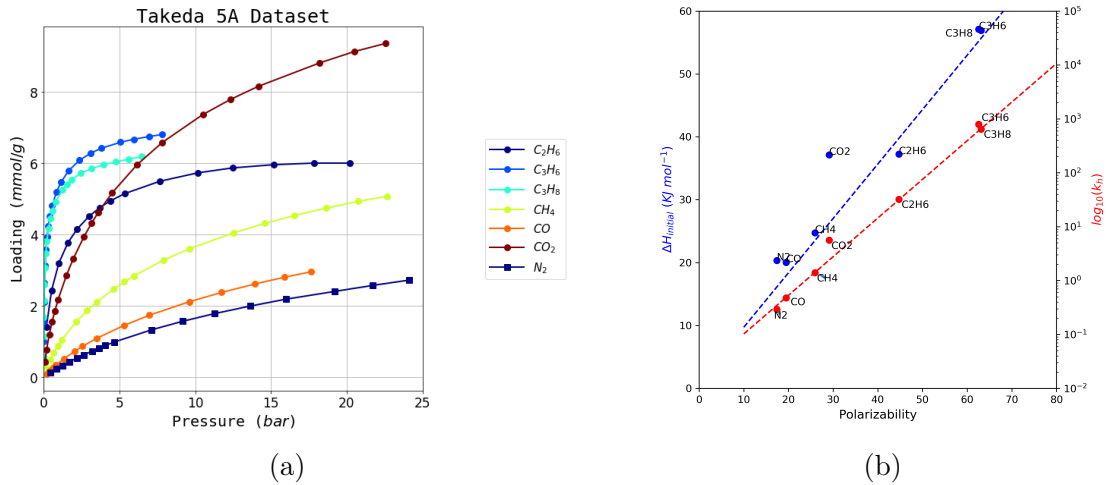


Figure 1.4: Takeda 5A dataset processing: (a) the experimental dataset all recorded gases and (b) the calculated trends of initial heat of adsorption and Henry's constant

one with the lowest residuals between the fitted function and the real data. Currently, the models available in pyGAPS are: Henry, single, double and triple site Langmuir,<sup>(14)</sup> BET,<sup>(12)</sup> Quadratic,<sup>(6)</sup> Jensen-Seaton,<sup>(5)</sup> Toth,<sup>(25)</sup> Tempkin approximation,<sup>(8)</sup> Virial,<sup>(9)</sup> and the Flory-Huggins<sup>(11)</sup> and Wilson<sup>(10)</sup> variations of Vacancy Solution Theory (VST). The isotherms and their best-fitting model is displayed in Figure 1.5a for the CO<sub>2</sub>-N<sub>2</sub> pair and in Figure 1.6a for the C<sub>3</sub>H<sub>8</sub>-C<sub>3</sub>H<sub>6</sub> pair.

#### Listing 1.2: Guessing the best model

```
model = pygaps.ModelIsotherm.from_pointisotherm(iso, guess_model=True)
```

For the carbon dioxide separation, we simulate all equilibrium points for the adsorbed and gaseous phases at different concentrations of the two gases at 1 bar. To do this we use the pygaps.iast\_vle() function which produces an analogue of a vapour-liquid equilibrium at a specified pressure for a binary mixture. The resulting graph of this function can be seen in Figure 1.6b. As expected, the predicted adsorbed mixture is rich in carbon dioxide. Selectivity can also be calculated in a single point, with the value at 15% CO<sub>2</sub> and 1 bar being 16.5.

For the propane-propylene separation, we simulate the selectivity for propane within a pressure range for a 50% mixture of the two gases. It can be seen that there is little or no preference for the unsaturated molecule, though the selectivity increases slightly at pressures above 1 bar.

## 1.5 Conclusion

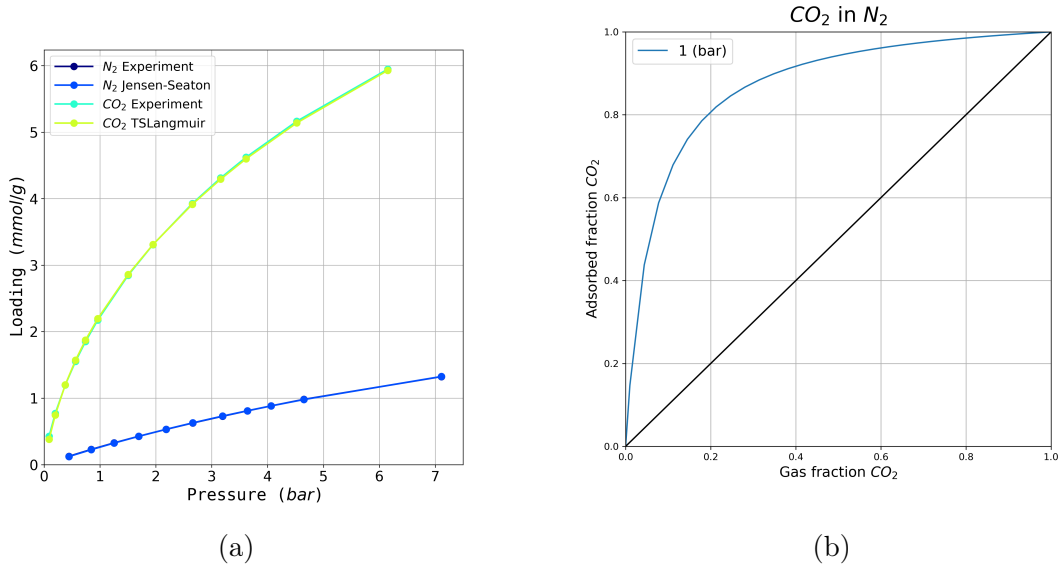


Figure 1.5: Modelling binary adsorption of  $CO_2$  and  $N_2$ : (a) the pure component isotherms and their best fit models and (b) the predicted composition of the gaseous and adsorbed phase for different fractions of  $CO_2$  at 1 bar

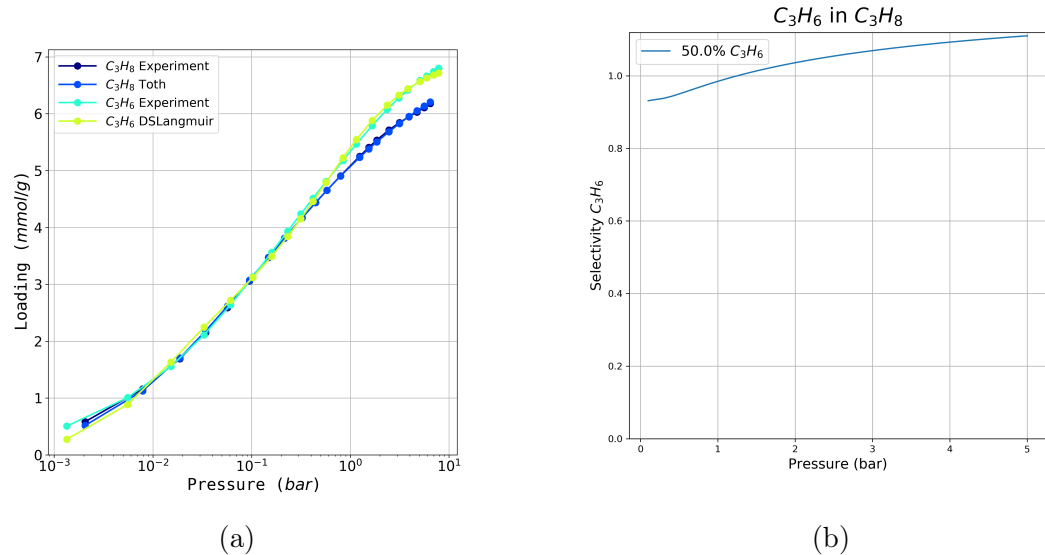


Figure 1.6: Modelling binary adsorption of a propane-propylene mixture: (a) the pure-component isotherms and their best fit models and (b) the predicted selectivity of propane adsorption of a 50-50% mixture in a range of pressure from 0.1 to 7 bar

# Bibliography

- [1] Elliott P. Barrett, Leslie G. Joyner, and Paul P. Halenda. The Determination of Pore Volume and Area Distributions in Porous Substances. I. Computations from Nitrogen Isotherms. *Journal of the American Chemical Society*, 73(1):373–380, January 1951. ISSN 0002-7863. doi: 10.1021/ja01145a126.
- [2] N.A. Seaton, J.P.R.B. Walton, and N. quirke. A new analysis method for the determination of the pore size distribution of porous carbons from nitrogen adsorption measurements. *Carbon*, 27(6):853–861, 1989. ISSN 00086223. doi: 10.1016/0008-6223(89)90035-3.
- [3] P. Tarazona, U. Marini Bettolo Marconi, and R. Evans. Phase equilibria of fluid interfaces and confined fluids: Non-local versus local density functionals. *Molecular Physics*, 60(3):573–595, February 1987. ISSN 0026-8976, 1362-3028. doi: 10.1080/00268978700100381.
- [4] Dan Siderius, Vincent Shen, and Russell Johnson. NIST / ARPA-E Database of Novel and Emerging Adsorbent Materials, NIST Standard Reference Database 205, 2015.
- [5] C. R. C. Jensen and N. A. Seaton. An isotherm equation for adsorption to high pressures in microporous adsorbents. *Langmuir*, 12(11):2866–2867, 1996.
- [6] Terrell L. Hill. *An Introduction to Statistical Thermodynamics*. Dover Publications, New York, 1986. ISBN 978-0-486-65242-9.
- [7] Mikhail Temkin. Kinetics of ammonia synthesis on promoted iron catalyst. *Acta Phys. Chim. USSR*, 12:327–356, 1940.
- [8] Cory M. Simon, Jihan Kim, Li-Chiang Lin, Richard L. Martin, Maciej Haranczyk, and Berend Smit. Optimizing nanoporous materials for gas storage. *Physical Chemistry Chemical Physics*, 16(12):5499, 2014. ISSN 1463-9076, 1463-9084. doi: 10.1039/c3cp55039g.
- [9] Alan L. Myers. Thermodynamics of adsorption in porous materials. *AICHE Journal*, 48(1):145–160, January 2002. ISSN 00011541. doi: 10.1002/aic.690480115.
- [10] Solot Suwanayuen and Ronald P. Danner. A gas adsorption isotherm equation based on vacancy solution theory. *AICHE Journal*, 26(1):68–76, January 1980. ISSN 00011541. doi: 10.1002/aic.690260112.
- [11] T. W. Cochran, R. L. Kabel, and R. P. Danner. Vacancy solution theory of adsorption using Flory-Huggins activity coefficient equations. *AICHE Journal*, 31(2):268–277, February 1985. ISSN 0001-1541, 1547-5905. doi: 10.1002/aic.690310214.

## Bibliography

- [12] Stephen Brunauer, P. H. Emmett, and Edward Teller. Adsorption of Gases in Multimolecular Layers. *Journal of the American Chemical Society*, 60(2):309–319, February 1938. ISSN 0002-7863, 1520-5126. doi: 10.1021/ja01269a023.
- [13] Jean Rouquerol, Françoise Rouquerol, Philip L. Llewellyn, Guillaume Maurin, and Kenneth Sing. *Adsorption by Powders and Porous Solids : Principles, Methodology and Applications*. 2013. ISBN 978-0-08-097035-6.
- [14] Irving Langmuir. The Adsorption of Gases on Plane Surfaces of Glass, Mica and Platinum. *Journal of the American Chemical Society*, 40(9):1361–1403, September 1918. ISSN 0002-7863, 1520-5126. doi: 10.1021/ja02242a004.
- [15] B Lippens. Studies on pore systems in catalysts V. The t method. *Journal of Catalysis*, 4(3):319–323, June 1965. ISSN 00219517. doi: 10.1016/0021-9517(65)90307-6.
- [16] D. Atkinson, A.I. McLeod, and K. S. W. Sing. Adsorptive properties of microporous carbons: Primary and secondary micropore filling. *Journal de Chimie Physique*, 81: 791–794, 1984. ISSN 0021-7689. doi: 10.1051/jcp/1984810791.
- [17] Geza Horvath and Kunitaro Kawazoe. Method for the calculation of effective pore size distribution in molecular sieve carbon. *Journal of Chemical Engineering of Japan*, 16(6):470–475, 1983. ISSN 1881-1299. doi: 10.1252/jcej.16.470.
- [18] Ian H. Bell, Jorrit Wronski, Sylvain Quoilin, and Vincent Lemort. Pure and Pseudo-pure Fluid Thermophysical Property Evaluation and the Open-Source Thermophysical Property Library CoolProp. *Industrial & Engineering Chemistry Research*, 53 (6):2498–2508, February 2014. ISSN 0888-5885, 1520-5045. doi: 10.1021/ie4033999.
- [19] Eric Lemmon. NIST Reference Fluid Thermodynamic and Transport Properties Database: Version 9.0, NIST Standard Reference Database 23, 1989.
- [20] Jasmina Hafizovic Cavka, Søren Jakobsen, Unni Olsbye, Nathalie Guillou, Carlo Lamberti, Silvia Bordiga, and Karl Petter Lillerud. A New Zirconium Inorganic Building Brick Forming Metal Organic Frameworks with Exceptional Stability. *Journal of the American Chemical Society*, 130(42):13850–13851, October 2008. ISSN 0002-7863. doi: 10.1021/ja8057953.
- [21] Andrew D. Wiersum, Estelle Soubeyrand-Lenoir, Qingyuan Yang, Beatrice Moulin, Vincent Guillerm, Mouna Ben Yahia, Sandrine Bourrelly, Alexandre Vimont, Stuart Miller, Christelle Vagner, Marco Daturi, Guillaume Clet, Christian Serre, Guillaume Maurin, and Philip L. Llewellyn. An Evaluation of UiO-66 for Gas-Based Applications. *Chemistry - An Asian Journal*, 6(12):3270–3280, December 2011. ISSN 18614728. doi: 10.1002/asia.201100201.

## Bibliography

- [22] Loredana Valenzano, Bartolomeo Civalleri, Sachin Chavan, Silvia Bordiga, Merete H. Nilsen, Søren Jakobsen, Karl Petter Lillerud, and Carlo Lamberti. Disclosing the Complex Structure of UiO-66 Metal Organic Framework: A Synergic Combination of Experiment and Theory. *Chemistry of Materials*, 23(7):1700–1718, April 2011. ISSN 0897-4756. doi: 10.1021/cm1022882.
- [23] A. Saito and H. C. Foley. Curvature and parametric sensitivity in models for adsorption in micropores. *AIChE Journal*, 37(3):429–436, March 1991. ISSN 0001-1541. doi: 10.1002/aic.690370312.
- [24] Cory M. Simon, Berend Smit, and Maciej Haranczyk. PyIAST: Ideal adsorbed solution theory (IAST) Python package. *Computer Physics Communications*, 200: 364–380, 2016. ISSN 00104655. doi: 10.1016/j.cpc.2015.11.016.
- [25] Jozsef Toth. Uniform Interpretation of Gas/Solid Adsorption. page 239.

## 2Extending bulk analysis of porous compounds through calorimetry

### 2.1 Introduction



### 2.2 Literature

### 2.3 Method

Gas adsorption isotherms and enthalpies were measured experimentally using a Tian-Calvet type microcalorimeter coupled with a home-made manometric gas dosing system.<sup>(1)</sup> This apparatus allows the simultaneous measurement of the adsorption isotherm and the corresponding differential enthalpies. Gas is introduced into the system using a step-by-step method and each dose is allowed to stabilize in a reference volume before being brought into contact with the adsorbent located in the microcalorimeter. The introduction of the adsorbate to the sample is accompanied by an exothermic thermal signal, measured by the thermopiles of the microcalorimeter. The peak in the calorimetric signal is integrated over time to give the total energy released during this adsorption step. At low coverage the error in the signal can be estimated to around  $\pm 0.2 \text{ kJ mol}^{-1}$ . Around 0.4 g of sample is used in each experiment. For each injection of gas, equilibrium was assumed to have been reached after 90 minutes. This was confirmed by the return of the calorimetric signal to its baseline ( $<5 \mu\text{W}$ ). The gases used for the adsorption were obtained from Air Liquide and were of minimum N47 quality (99.997 % purity).

### 2.4 Results and discussion

### 2.5 Conclusion

# Bibliography

- [1] Philip L. Llewellyn and Guillaume Maurin. Gas adsorption microcalorimetry and modelling to characterise zeolites and related materials. *Comptes Rendus Chimie*, 8 (3-4):283–302, March 2005. ISSN 16310748. doi: 10.1016/j.crci.2004.11.004.

# **3Exploring the impact of synthesis and defects on adsorption measurements**

## **3.1 Introduction**



## **3.2 Literature**

## **3.3 Method**

## **3.4 Results and discussion**

## **3.5 Conclusion**

# Bibliography

# 4 Exploring the impact of material form on adsorption measurements

## 4.1 Introduction

An adsorbent cannot be used in an industrial process in its raw powder form. The small crystals which are normally the synthesis product of such a material would not be suited for direct use and need to be transformed into hierarchically porous structures.

Therefore, adsorbents are usually shaped into pellets, a process which introduces a range of benefits, such as improved flow regimes, better thermal management and material containment. The shaping process is needed not just for stabilising the small particles, but also to impart the resulting pellet with a high enough mechanical resistance to withstand the stresses imposed by the high flow encountered in an industrial bed.

The shaping process is therefore a crucial step towards the large-scale use of an adsorbent material. Even for commonplace adsorbents such as carbons and zeolites, the optimum binding compound and the shaping process itself are the subject of extensive research. Often, the procedure is tailored for individual material and application.

In an ideal setting, the process has limited effects on the properties of the material. However, this is often not the case, as shaping can degrade or improve adsorption performance. After a short introduction to shaping, this chapter explores the variability introduced by the binder in three topical MOFs: UiO-66(Zr), MIL-100(Fe) and MIL-127(Fe), which have been selected for their good stability and well-studied adsorption behaviour. The alumina shaped variant of these MOFs is compared to the original powder material, with regard to the adsorption of a series of common gasses and vapours. Microcalorimetry in conjunction with 8 gas probes has been used to get an in-depth picture of the change in surface energetics, with a separate study of adsorption of water and methanol vapour to examine changes in hydrophobicity. Particular behaviours are then highlighted and discussed.

Finally, a previous study on the same materials shaped with a poly-vinyl alcohol (PVA) binder is extended to vapour adsorption and the entire dataset is processed to obtain an overview of the impact of a hydrophobic and a hydrophilic binder on adsorption performance.

## 4.2 Shaping in context

In order to use an adsorbent in an industrial setting such as the beds and columns common in PSA (pressure swing adsorption) and TSA (temperature swing adsorption) processes, a pelletized form of the material is required.<sup>(1)</sup>

The kinetics of the adsorption process are generally improved by the multi-scale pore size distribution afforded through shaping. Capacity per mass of pellet is expected to

decrease due to the addition of a non-porous component, but the difference should be small and should not arise due to effects such as pore blocking or pore filling with the binder material. Furthermore, the densification effect is expected to lead to better performance on a volume basis. Finally, binder addition should not influence the chemical properties of the adsorbent, and preserve the original interactions with the adsorbate. With a judicious choice of binding material, the resulting pellet should outperform the powder.

For carbons, binders such as pitch, polymers (CMC, PVA) or even non-porous carbon black are commonly used.<sup>(2)</sup> Often, a combination of binders is used, each with a different task during the pelletization process.<sup>(3)</sup> The process itself consists of extrusion of the particle-binder slurry and then hardening either through temperature, cross-linking or chemical treatment. Other methods, such as spray-drying or granulation can similarly be used.<sup>(4)</sup>

shaping  
meth-  
ods

For zeolites, inorganic binders are more prevalent, with silica, alumina and clay binders commonly used in industry. It has been shown<sup>(5,6)</sup> that the choice of binder can introduce large property variations, ranging from loss of porosity and structure to the enhancement of the desired reactivity and selectivity through changes in the acid site density or ion migration.

The shaping of MOFs has been attempted with a wide range of binders and methods. Methods such as granulation, spray-drying or extrusion have all been successfully employed to create MOF pellets.<sup>(7)</sup> Monoliths have also been shown to be an effective way for shaping purposes, either through impregnation<sup>(8)</sup> or through support on alumina.<sup>(9)</sup> Surprisingly, compression<sup>(10)</sup> or even simple air drying of MOF slurries<sup>(11)</sup> have also shown good results. Note that the ZIF-8 monolith prepared through the latter method had a three times larger volumetric specific surface area than the conventional powder.

The connection between MOF and binder is also of crucial importance for membranes. The MOF-polymer interface has been shown<sup>(12)</sup> to be subject to a complex interplay of interactions between the organic chains and the crystal surfaces. These effects can be striking enough to warrant further research into MOF-polymer hybrids,<sup>(13)</sup> with the aim of combining the unique attributes of both materials.

Previous work from this group<sup>(14)</sup> has analysed the impact of PVA shaping on a series of MOFs. It was shown that the binder did introduce some specific effects, such as a protection effect on the reduction of  $\text{Fe}^{3+}$  to  $\text{Fe}^{2+}$  in MIL-127(Fe), as well as a curious gating effect seen on butane adsorption on MIL-100(Fe), likely due to polymer chains covering pore entrances. Otherwise, the shaping imparted good performance to the shaped samples, with almost no capacity loss on a mass basis. Unfortunately, the use of a polymer limited the activation temperature of the samples to a maximum of 150 °C.

In this work we have selected the same series of “topical” MOFs and have investigated the influence of a different shaping method, namely the use of alumina binder, on their adsorption properties.

The UiO-66(Zr) MOF and its derivatives are well known due to their stability, both in regards to temperature and chemical compounds.<sup>(15)</sup> It is composed of Zr6-oxo clusters which are connected with benzene dicarboxilate (BDC) linkers to form a face-centered

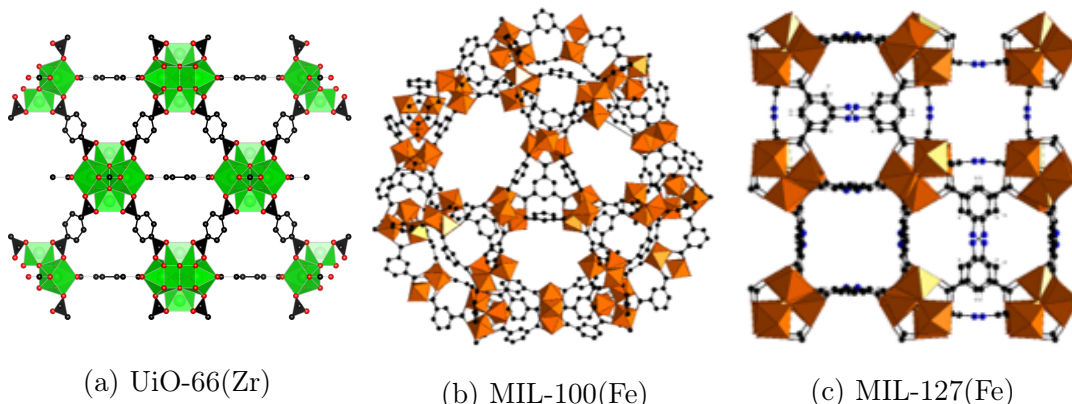


Figure 4.1: The unit structures of the investigated MOFs. The colour coding is as follows: Zr polyhedra in green, Fe octahedra in brown, C in black, O in red, N in blue. Hydrogen atoms are omitted for clarity.

cubic framework. It has shown promise<sup>(16)</sup> in use for gas adsorption applications.

MIL-100(Fe) is a MOF which uses the benzene tricarboxilate (BTC) linker in conjunction with trimeric iron (III) octahedral clusters.<sup>(17)</sup> The framework assembles in hybrid supertetrahedra which leads to very large pore sizes. The iron trimers are coordinated with anions and have shown a propensity to partially reduce to a divalent  $\text{Fe}^{2+}$  state, exposing a naked metal site in the process.<sup>(18)</sup>

The last material, MIL-127(Fe), originally reported by Liu et al. is a MOF built from the same metal (III) octahedra trimers as MIL-100(Fe), but using the 3,3',5,5'-azobzenenetetracarboxylate (TazBz) linker, to produce a framework with the (soc) topology. This material has shown promise<sup>(20)</sup> for large scale synthesis. Furthermore, due to its alternating hydrophobic/hydrophilic microporous systems, it has been shown to be of interest for multiple applications such as catalysis or CO<sub>2</sub> capture.<sup>(21)</sup>

The structures of the three materials can be seen in Figure 4.1.

### 4.3 Synthesis, shaping and characterisation

#### 4.3.1 Material Synthesis

The synthesis of these MOFs is well described in literature, as it has been previously reported for UiO-66(Zr)<sup>(15)</sup> and MIL-100(Fe).<sup>(22)</sup>

The UiO-66(Zr) and MIL-100(Fe) powders have been synthesised at the Korea Research Institute of Chemical Technology (KRICT) according to the methods previously referenced. Complete details of the synthesis method can be found in the related publication<sup>(23)</sup> and in Appendix 5.

### 4.3.2 Shaping Procedure

The shaping of the samples also took place at KRICT and was done using a wet granulation method. In the case of the alumina binder, the MOF powder was mixed with the previously prepared mesoporous  $\rho$ -alumina with water added as the dispersing medium. For the PVA binder, the MOF powder was instead added to a solution of ethanol solution containing a polymer mixture of polyvinyl groups such as polyvinyl alcohol and polyvinyl butyral. The resulting mixture was shaped into beads using a hand-made pan granulator. During the process, the spheres were sprayed with the respective solvent in order to achieve desired size. The beads were then sieved and rolled using a roller machine to enhance their spherical shape. Finally, the prepared samples were dried at 303 K for 12 h to remove all residual solvent. The resulting beads were near spherical in shape, with a diameter between 2 mm to 2.5 mm.

### 4.3.3 Characterisation of powders and pellets

The primary interest of the study was observing differences in adsorption properties between the powder and the shaped materials.

Thermogravimetric analysis was used to verify that the binder did not change the thermal stability of the materials and, in the case of the PVA variant, to ensure that the activation temperature chosen did not induce polymer decomposition. The TGA method is described in detail in Appendix 1.

### 4.3.4 Sample activation for adsorption

The materials were pre-treated before all adsorption experiments by activation at high temperature under secondary vacuum for 16 hours. The activation temperature was specific to each solid: 200 °C for UiO-66(Zr), 150 °C for MIL-100(Fe) and 150 °C for MIL-127(Fe).

## 4.4 Results and discussion

### 4.4.1 Thermal stability

In order to check if the shaped samples have not undergone bulk structural changes, as well as find a suitable activation temperature, the powder and shaped samples underwent thermogravimetric analysis under an argon atmosphere.

The process of shaping did not have any impact on the thermal stability of the investigated MOFs, as evidenced by the TGA curves in Figure 4.2. The primary mass loss occurs in a 10 °C range for all powder-pellet pairs. Shaped samples are also seen to have a smaller mass loss at high temperatures. This is expected, as after the addition of temperature inert alumina, the MOF makes up a lower percentage of the material.

4 Exploring the impact of material form on adsorption measurements

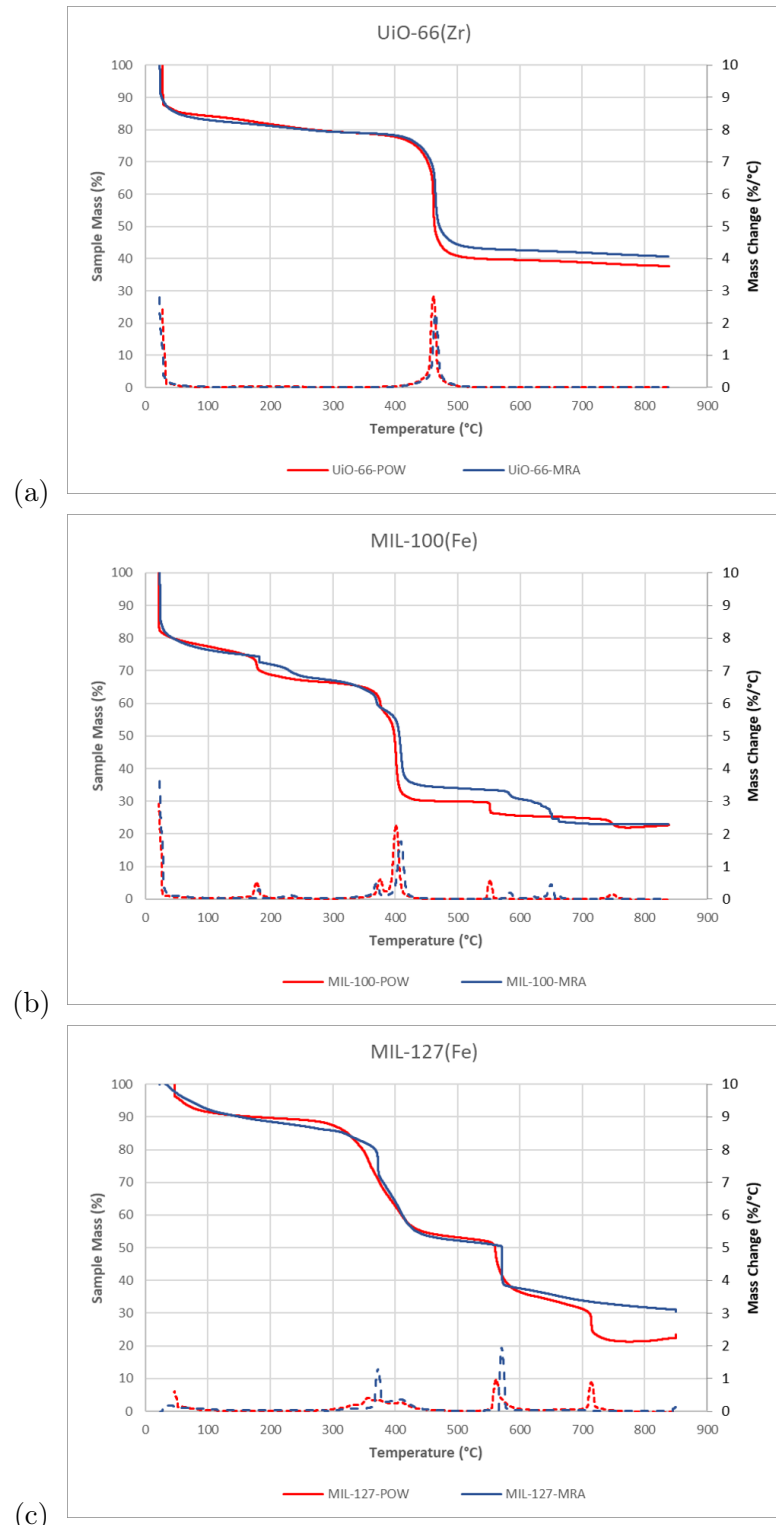


Figure 4.2: High resolution TGA curves recorded under argon on (a) UiO-66(Zr), (b) MIL-100(Fe) and (c) MIL-127(Fe). The original powders are depicted in red and the shaped material in blue.

#### 4.4.2 Adsorption isotherms at 77K and room temperature

Nitrogen sorption isotherms measured at 77K have been measured on both powder and  $\rho$ -alumina pellets, with the isotherms presented in Figure 4.3. Observation of the physisorption curves sheds light on the impact of the alumina binder on the materials chosen. The shapes of all isotherms are visually similar, with the pellet curves shifted downwards due to the aforementioned structure degradation. In both powders and pellets, the increased uptake after  $0.9 \text{ } p/p^0$  is a sign of condensation in very large pores or voids, which can be attributed to intra-pellet spaces and crystal agglomeration. In the MIL-127(Fe) pellets, a narrow hysteresis curve is seen, which closes at a  $p/p^0$  of 0.5. This curve corresponds to capillary condensation in a pore size of around 4 nm. This pore width is too small to be a sign of inter-pellet voids and therefore must be a consequence of the shaping process.

While no other significant features are visible on the isotherms themselves, we use pyGAPS to further process them and obtain properties such as specific surface area, calculated through the BET method and pore volume, calculated as the volume of nitrogen adsorbed at a  $p/p^0$  of 0.2. As the surface area of the binder is lower than the one of the MOF, a drop in both these properties is expected. The calculated values are shown in Table 4.1.

Table 4.1: Properties of the studied powders and pellets

MOF	form	BET surface area	Pore volume	Bulk density
UiO-66(Zr)	powder	903	0.38	0.3192
	$\rho$ -alumina	619	0.24	0.4724
MIL-100(Fe)	powder	1928	0.78	0.2165
	$\rho$ -alumina	1451	0.6	0.3512
MIL-127(Fe)	powder	1400	x	0.412
	$\rho$ -alumina	1266	0.49	0.526

As predicted, the specific surface area of the shaped samples is decreased compared to the corresponding powder. While in the case of MIL-127(Fe) the BET area is only 10% lower, for the MIL-100(Fe) and UiO-66(Zr) materials a larger drop is seen, of 25% and 31%, respectively. A similar decrease can be seen in pore volume, with a 36%, 23% and x% loss seen in UiO-66(Zr), MIL-100(Fe) and MIL-127(Fe) respectively. The decrease in both surface area and micropore volume is too large for it to be a consequence of the presence of non-porous binder. It is therefore theorised that some structure degradation must have occurred during the pelletisation process. Despite a loss in surface area, the bulk density of the material has increased, due to crystal aggregation.

#### 4.4.3 Room temperature gas adsorption and microcalorimetry

As previously shown, combining microcalorimetry with adsorption manometry can give an insight into the energetics of the adsorption process by directly measuring differential

some  
microp-  
ore vol-  
umes  
miss-  
ing +  
density

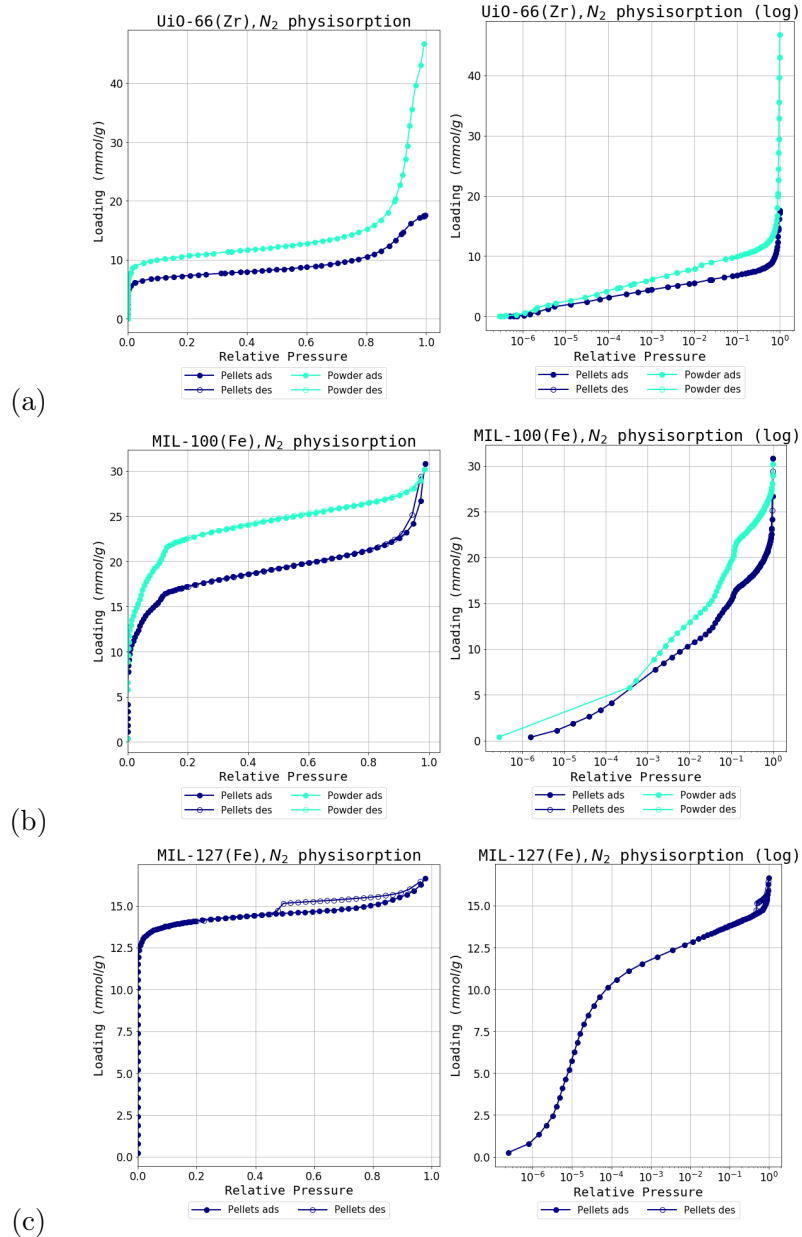


Figure 4.3: Nitrogen isotherms at 77K for (a) UiO-66(Zr), (b) MIL-100(Fe) and (c) MIL-127(Fe). The powder sample is in light blue while the  $\rho$ -alumina sample in dark blue. Logarithmic graphs of the isotherms are on the right for clarity of the low pressure region.

heat. Even though the different contributions to the overall enthalpy curve cannot be decoupled from the individual sources, such as guest-host interactions or fluid-fluid interactions, it can be successfully applied to observing the effect of a process or treatment such as shaping on the properties of a MOF.

Eight probe gasses have been chosen for adsorption at 303 K: N<sub>2</sub>, CO, CO<sub>2</sub>, CH<sub>4</sub>, C<sub>2</sub>H<sub>6</sub>, C<sub>3</sub>H<sub>6</sub>, C<sub>3</sub>H<sub>8</sub> and C<sub>4</sub>H<sub>10</sub>. The range of adsorbates chosen allows different effects to be investigated. The adsorption of saturated hydrocarbons with an increasing carbon number (C1-C4) can be assumed to be driven strictly by Van-der-Waals forces, due to the shielding effects of the hydrogen atoms. Differences in the maximum uptakes of these gasses will point to loss of porosity or crystallinity. A capacity loss with an increasing carbon number will point to size exclusion effects induced by the binder, such as particle coating, pore filling or pore obstruction. The other probes have been chosen for their properties which can shine light on other specific interaction types present during the adsorption. Carbon monoxide is a slightly dipolar molecule which has the ability to act as an with other charges in the pores. It also can highlight CUS (coordinatively unsaturated sites) generated through defects, reduction or open metal sites due to its propensity for  $\pi$  backbonding coordination. This electron transfer process can also result in complexation with molecular orbitals in systems with  $\pi$  bonds such as alkenes and alkynes. Propylene is used as an unsaturated hydrocarbon probe gas for this purpose. Carbon dioxide is a highly quadrupolar molecule which will be strongly adsorbed in polar pore environments. Changes in the adsorption behaviour of CO<sub>2</sub> will shed light on such surface changes and can even be used as a predictor of hydrophobicity.<sup>(21)</sup> Finally, N<sub>2</sub> is a staple adsorbent for material characterisation when used at 77 K. The molecule is a slight quadrupole and has also been shown to chelate to some transitional metals in an analogue fashion to CO.

To eliminate the influence of kinetic and diffusion effects on the experiments, care has been taken to allow time for complete equilibration of both pressure and calorimeter signal. The complete dataset of adsorption isotherms, in the basis of both mass and volume can be found in Appendix 5.

After collecting the combined isotherm and enthalpy data, three indicators have been chosen to best represent the effects of shaping: initial enthalpy of adsorption, initial Henry constant and maximum capacity. These numeric performance indicators have been calculated using the available functionality in pyGAPS.

The initial enthalpy of adsorption extrapolated at zero coverage is a measure of the interaction with highest energetic sites on the MOF surface. Conversely, the initial Henry constant ( $K_{Hi}$ ), here obtained through fitting the virial adsorption model as , is also an indication of adsorption in the pores before any layering or adsorbate-adsorbate interaction comes into effect. The last indicator, maximum capacity, was taken as the loading attained when the isotherm reached a plateau. In the case of probes where the plateau was outside the range of pressure of the instrumentation (>50 bar), the loading at the highest available pressure was considered as a suitable approximation. The three key performance indicators (KPIs) have then been compared side by side on both the powder and shaped samples.

reference  
to  
virial

### UiO-66(Zr)

A visual inspection of the enthalpy curves on as-synthesised UiO-66(Zr) show it to be relatively homogenous, with flat profiles being common. This is typical of this MOF, which has a pore environment without high energy adsorption sites.<sup>(16)</sup> Both CO<sub>2</sub> and CO show a higher enthalpy of adsorption at low loadings, as seen in Figure 4.4, which is likely due to their quadrupole and dipole interaction, respectively.

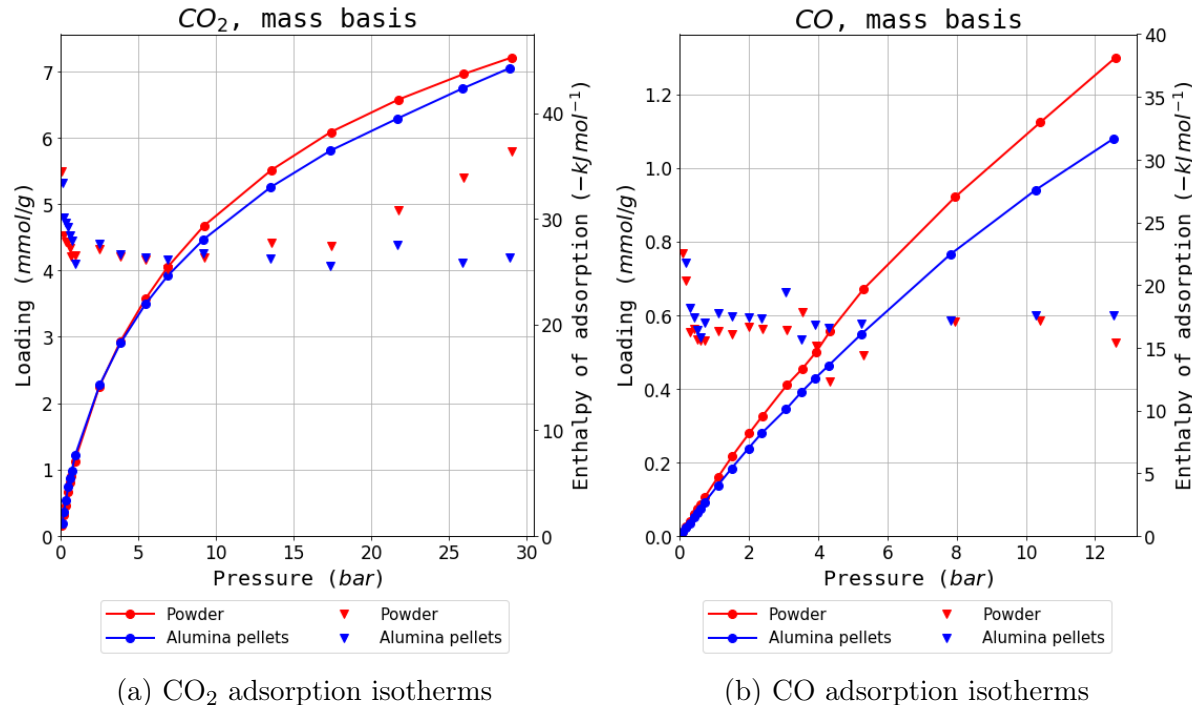


Figure 4.4: Selected isotherms from the UiO-66(Zr) dataset

The KPI graphs in Figure 4.5 show very similar values for both Henry's constant and initial enthalpy of adsorption. It is therefore apparent that the shaping process did not change the interaction of the adsorbate with the MOF surface.

The maximum capacity graphs show a more interesting trend. When using small adsorbates such as N<sub>2</sub>, CO<sub>2</sub> and CH<sub>4</sub>, the shaped samples have a similar performance on a mass basis and, due to the densification process, better capacities on a volume basis. Starting with ethane, the maximum capacity difference starts to increase, with lower performance as molecule size increases. On hydrocarbons with a carbon number of 3 and 4, both mass basis and volume basis capacity is decreased compared to the original powder. This size exclusion effect could be explained by the coating of crystal surfaces with the alumina binder.

It could also be argued that instead of size exclusion, the effect is due to an overall decrease in pore volume, and that the isotherms of the low molecular weight gasses will diverge at higher pressures as the pores are filled. A counterargument for this hypothesis is that in the case of CO<sub>2</sub>, the plateau is reached with no differences between the powder

and the pellet as seen in Figure 4.4a.

Carbon monoxide is an apparent outlier to this trend, with a decreased maximum capacity and a small molecular size. However, when looking at the isotherms directly (4.4b) it is obvious that the effect is likely to be due to experimental errors, considering the low amount adsorbed and the good overlap in the enthalpy curves.

Overall, the shaping performance of UiO-66(Zr) is reasonable, as long as only small adsorbates are used.

### MIL-100(Fe)

The enthalpy profiles on the MIL-100(Fe) powder are less homogenous than the ones on UiO-66(Zr). Some effects can be seen with probes which can interact with the partially reduced Fe(II) atom, such as carbon monoxide and propylene (Figure ??). Indeed, when comparing both the initial Henry constants and enthalpy of adsorption, for CO and C<sub>3</sub>H<sub>6</sub>, these are higher than the values obtained on UiO-66(Zr). With initial enthalpy of adsorption for CO of around 45 kJ mol<sup>-1</sup>, the value falls into the range of previous<sup>(18)</sup> results for interactions with such Fe(II) CUS.

Comparing the powder and shaped variants, there are no apparent differences between the two. The only discrepancy, which can be seen on the nitrogen initial  $K_H$  follows as a result of an ill-fitting virial parameter, and can be assumed an error after observing the isotherm overlap directly. It could be theorised that by activation at a higher temperature (250 °C), the percentage of iron trimers which would undergo reduction will increase and a further interaction could be observed. However, the activation temperature was chosen to allow comparisons with the PVA study,<sup>(14)</sup> where temperatures over 180 °C would lead to the burn-off of the polymer binder.

The maximum loading differences (Figure 4.7c) of MIL-100(Fe) show a very similar behaviour. On all probes tested, a fixed capacity loss of between 10-20% can be seen on a mass basis. However, the increase in density afforded by the compression during pelletisation leads to a compensation in performance as can be seen directly when looking at isotherms on mass and volume material basis in Figure ?? and Figure ?? respectively.

We can conclude that MIL-100(Fe) is almost unaffected by alumina shaping. A slight loss in maximum capacity on a mass basis is compensated by a pronounced densification, which is desirable in an industrial setting.

### MIL-127(Fe)

The isotherms on the original powder form of MIL-127(Fe) should show similar behaviour as on MIL-100(Fe), due to the presence of the same iron trimesate moieties, although with a sharper uptake as a result of the smaller pores. Enthalpy profiles are also influenced by the similar interactions with the iron CUS leading to higher initial heats of adsorption on CO and C<sub>3</sub>H<sub>6</sub>. An overall increase in the heat of adsorption at higher loadings is seen throughout the probe series, as seen for example on butane in Figure 4.8a. Due to the bimodal pore distribution in the MIL-127(Fe) structure, it is likely that adsorption first commences in the small ( $\sim 6 \text{ \AA}$ ) channels and then, at higher

#### 4 Exploring the impact of material form on adsorption measurements

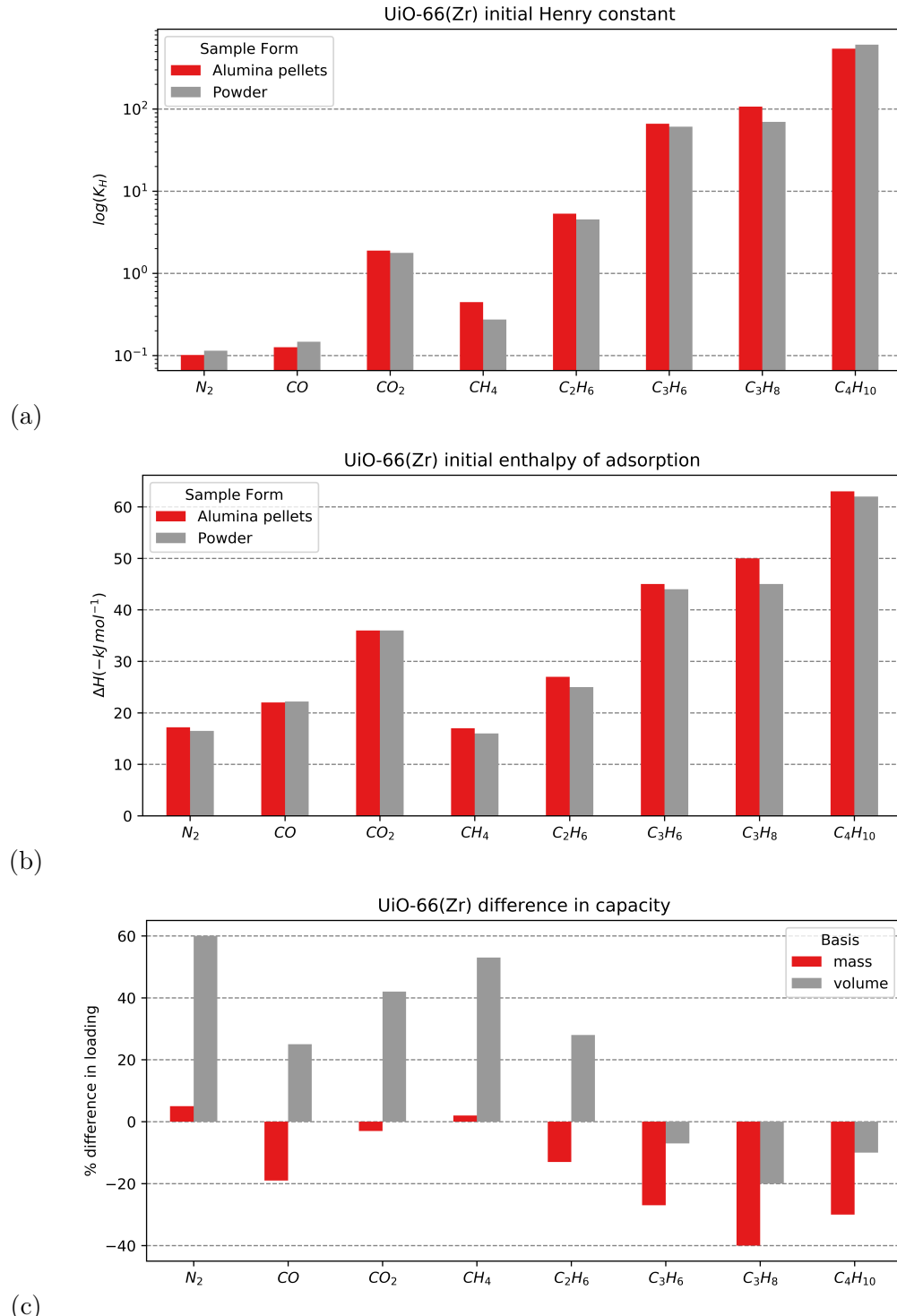


Figure 4.5: KPIs extracted from the UiO-66(Zr) adsorption dataset with (a) logarithmic initial Henry constant (b) initial enthalpy of adsorption and (c) change in adsorption maximum capacity from the powder to the alumina shaped version on a mass and volume basis in red and grey respectively

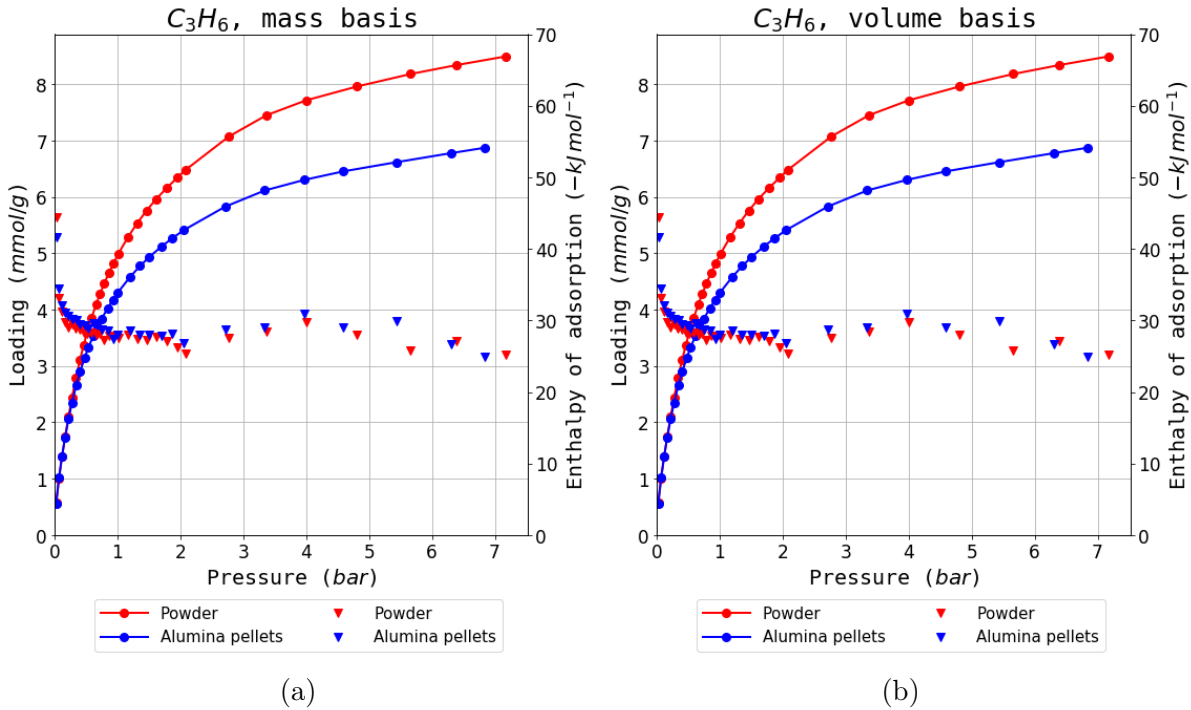


Figure 4.6: Propylene isotherms on MIL-100(Fe) on a (a) mass and (b) volume adsorbent basis.

pressures, intrusion into the larger cage-type pores is possible through the  $\sim 3 \text{ \AA}$  narrow apertures. The confined cages have an increased interaction with the molecule which leads to the higher enthalpy values.

When comparing the powder and the pellet variant with respect to initial Henry's constant, a large difference in  $K_H$  on CO stands out. The value of the initial enthalpy of adsorption does not follow the same pattern. However, visual inspection of the enthalpy curve in Figure 4.8b shows that the energy of adsorption corresponding to interactions with the more active sites is maintained for a larger percentage of the total coverage. This points to the higher preponderance of such sites in the powder variant. A similar offset can be seen in the propylene enthalpy at very low pressures, but this is not reflected in the shape of the isotherm. The weaker complexation strength and the larger size of the molecule likely limits the effect seen in the carbon monoxide isotherm. As for the underlying reason behind the isotherm divergence, it could be that the alumina binder acts as protection against the generation of iron(II) during thermal activation. No other differences are seen between the two forms on either Henry constant and initial enthalpy of adsorption.

The capacity comparison in Figure 4.9c paints an interesting picture. For most probes there is no change in maximum loading showing that there is no structure degradation or pore filling. Two outliers are apparent: carbon monoxide and butane. The decrease in capacity on CO can be explained through the aforementioned changes in active site prevalence. The drop in butane cannot be a consequence of the same effect as there is a

#### 4 Exploring the impact of material form on adsorption measurements

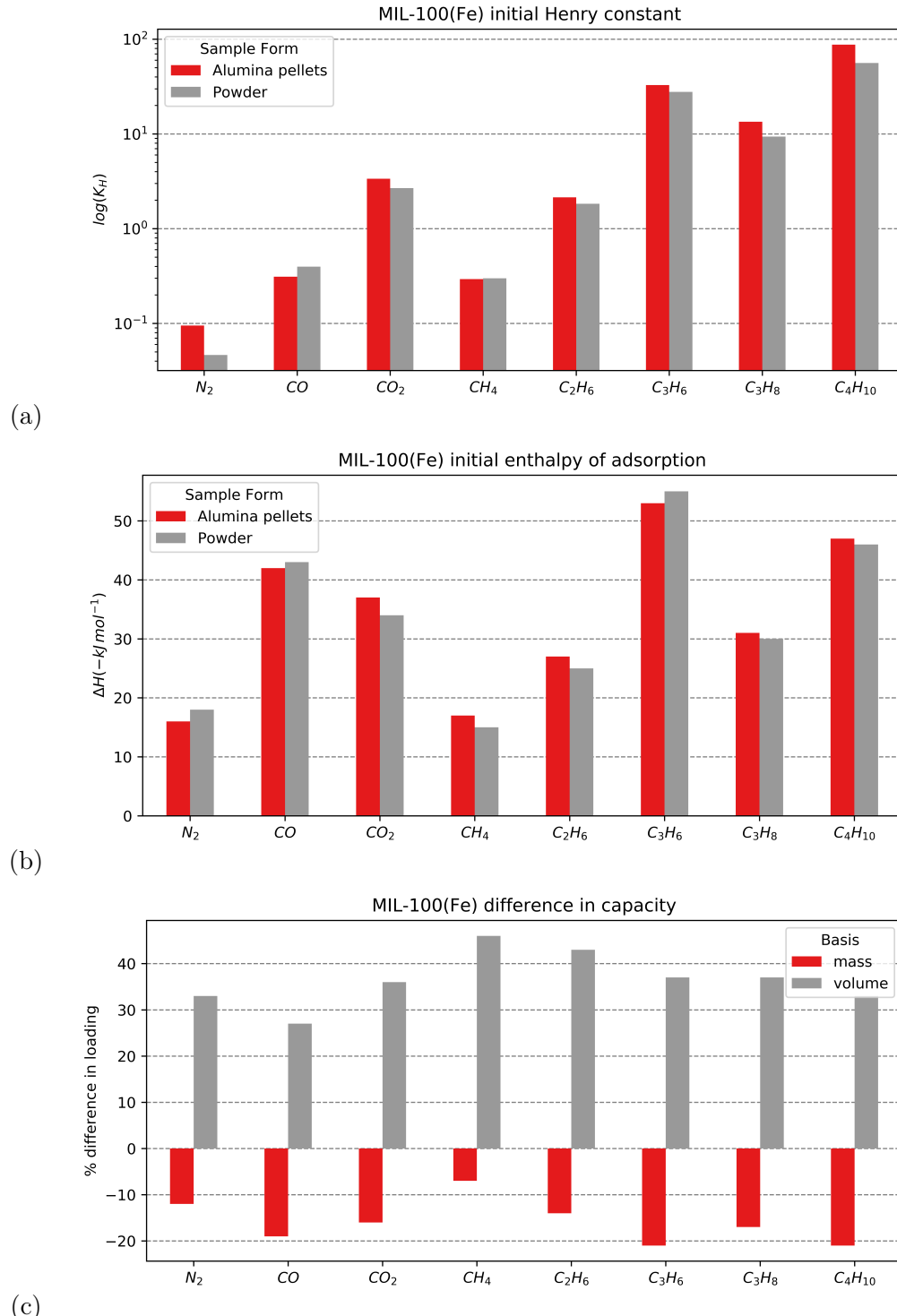


Figure 4.7: KPIs extracted from the MIL-100(Fe) adsorption dataset with (a) logarithmic initial Henry constant (b) initial enthalpy of adsorption and (c) change in adsorption maximum capacity from the powder to the alumina shaped version on a mass and volume basis in red and grey respectively

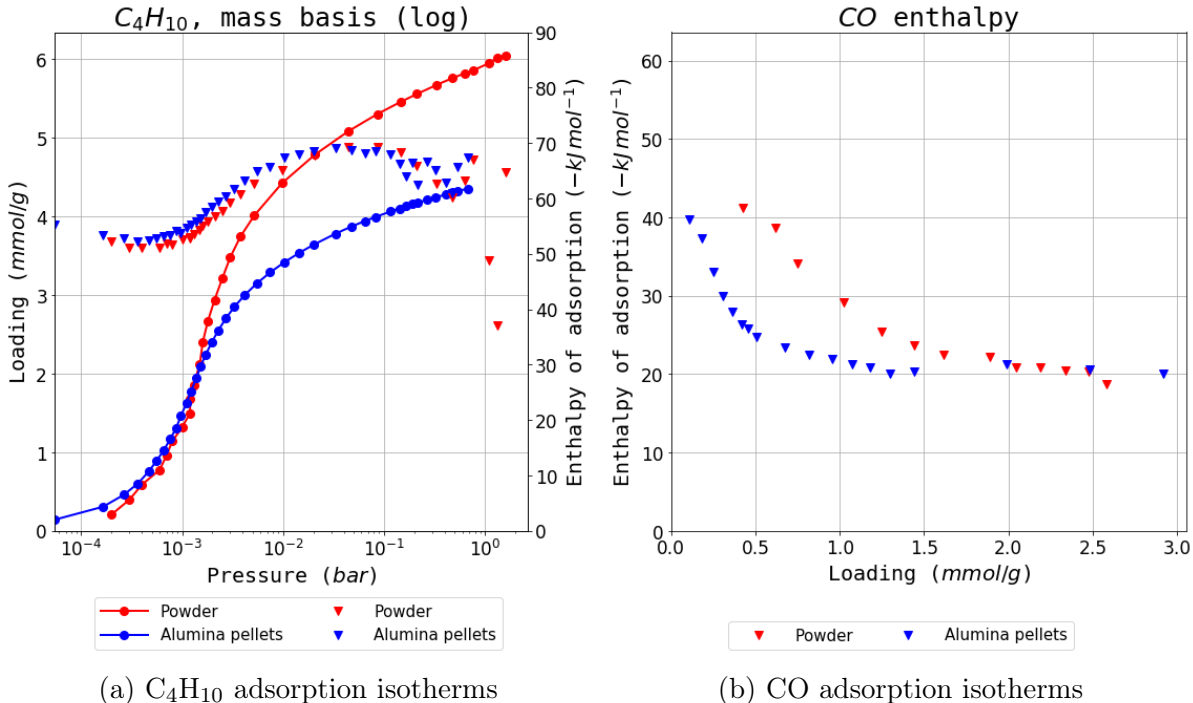


Figure 4.8: Selected isotherms from the MIL-127(Fe) dataset

perfect overlap in the enthalpy curves as seen in Figure 4.8a. Therefore it likely better explained through a size exclusion effect as seen on UiO-66(Zr).

Overall, MIL-127(Fe) shows excellent performance when undergoing alumina shaping, with almost no capacity loss, as long as carbon monoxide or butane adsorption are required, where specific effects come into play.

#### 4.4.4 Vapour adsorption

The effects of shaping with  $\rho$ -alumina are so far more subtle than the changes encountered when using PVA, as shown in the corresponding study.<sup>(14)</sup> The influence of the binder on hydrophobic character of the material may be of interest for tuning the properties of the beads. Adsorption of water and methanol vapour can serve as a probe for small changes in surface properties. To this end, the same PVA samples which were studied in the previous study were studied alongside the MRA-shaped MOF.

Due to its surface charges, alumina is a hydrophilic substance, with a contact angle of  $10^\circ$ . It is expected that its addition will therefore increase the affinity of the resulting pellet towards water. On the other hand, the PVA binder is more hydrophilic, with a water contact angle of  $51^\circ$ . The medium affinity for water is due to the surface hydroxyl functionalizations, which can lead to hydrogen bonding.

Two indicators may highlight changes in material hydrophilicity: adsorption in the low relative pressure region ( $p/p^0 < 0.3$ ) and condensation steps in the isotherm. The adsorption at low pressures is representative of the first interactions with the surface,

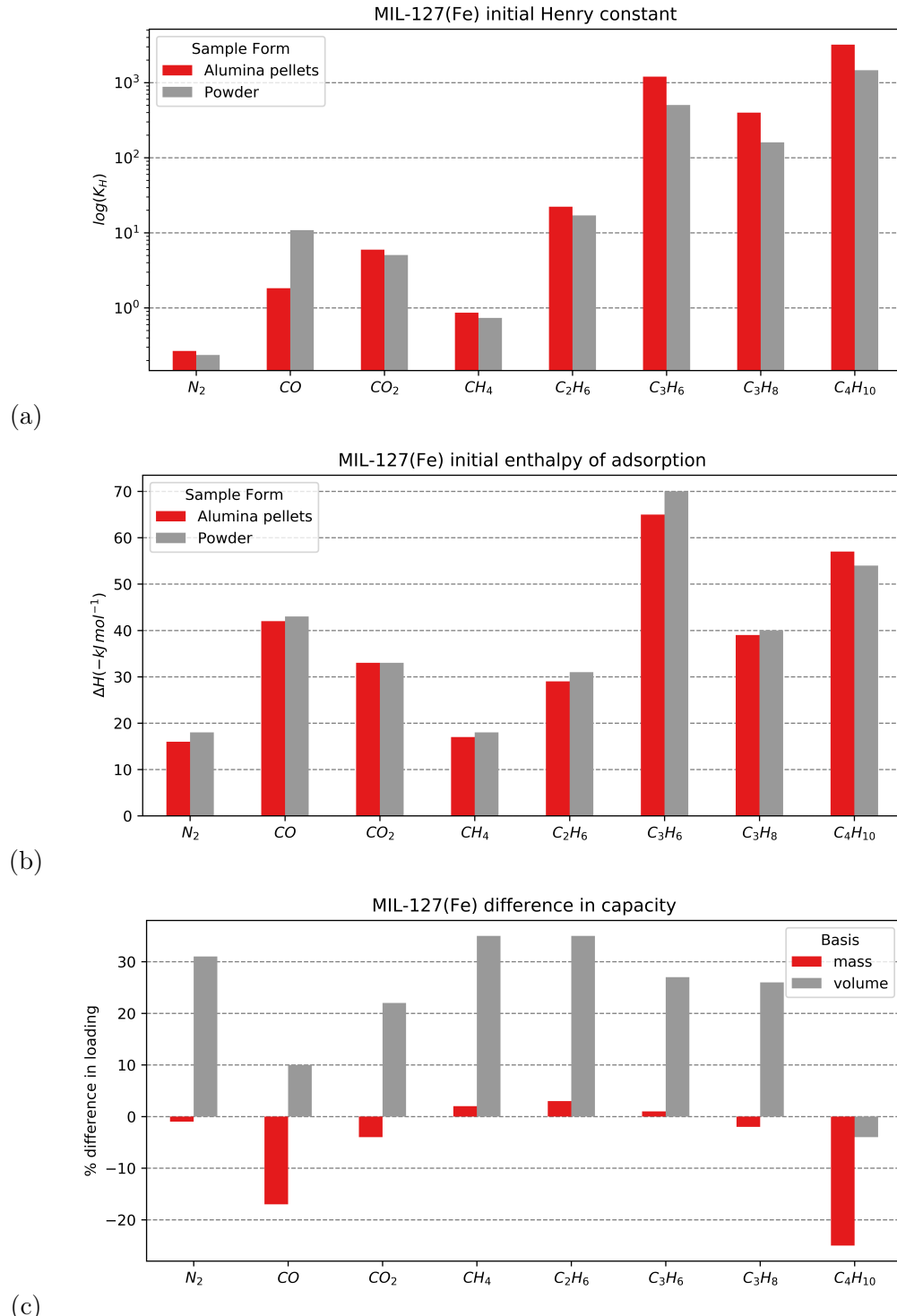


Figure 4.9: KPIs extracted from the MIL-127(Fe) adsorption dataset with (a) logarithmic initial Henry constant (b) initial enthalpy of adsorption and (c) change in adsorption maximum capacity from the powder to the alumina shaped version on a mass and volume basis in red and grey respectively

as explained in the previous sections. The pressure at which condensation occurs in the pores of the material, or where a sharp isotherm increase is seen depends on the size of the pore, but also on the pore environment and guest-guest interactions.

The measured isotherms on water and methanol can be found in Figure 4.10 and 4.11 respectively. The isotherms measured on the original powder materials show the normal adsorption behaviour which can then be compared with the MRA and PVA shaped samples.

On UiO-66(Zr), the water isotherm shows a slow uptake at the start, corresponding to a hydrophobic material and then shows a small step at  $p/p^0 = 0.3$ . Complete pore filling happens at  $p/p^0 = 0.8$ .

Water isotherms on MIL-100(Fe) show a more hydrophilic environment, with a higher initial uptake, and two condensation steps at  $p/p^0 = 0.3$  and  $p/p^0 = 0.5$ . There is pronounced hysteresis on the desorption branch. The methanol adsorption isotherms also show a two step adsorption isotherm, but without any hysteresis present. The shaped samples also show a lower

It can be therefore concluded that overall, the addition of either binder has not influenced the behaviour towards water or methanol for the materials studied. The full water adsorption isotherms can be found in Figure 4.10.

## 4.5 Conclusion

It can be concluded that the process of alumina shaping does not, in general, have an impact on the surface chemistry of the three MOF materials. Interestingly, in regards to the changes in maximum capacity, each material has its own particular behaviour: UiO-66(Zr) has a higher loss in capacity with larger molecular probes, MIL-100(Fe) has a decrease of 10-20% across all gasses and MIL-127(Fe) matches loading on a mass basis except on CO and C<sub>4</sub>H<sub>10</sub>.

The shaping also induces a densification which, in almost all cases, leads to a better performance on a volumetric basis. However, the influence on the mass transport effects of the alumina binder is not known and should be investigated further.

Overall, the process of alumina shaping is a promising method of preparing MOFs for gas-related applications in separation and storage, but care should be taken to not generalise the effects present on one material to another.

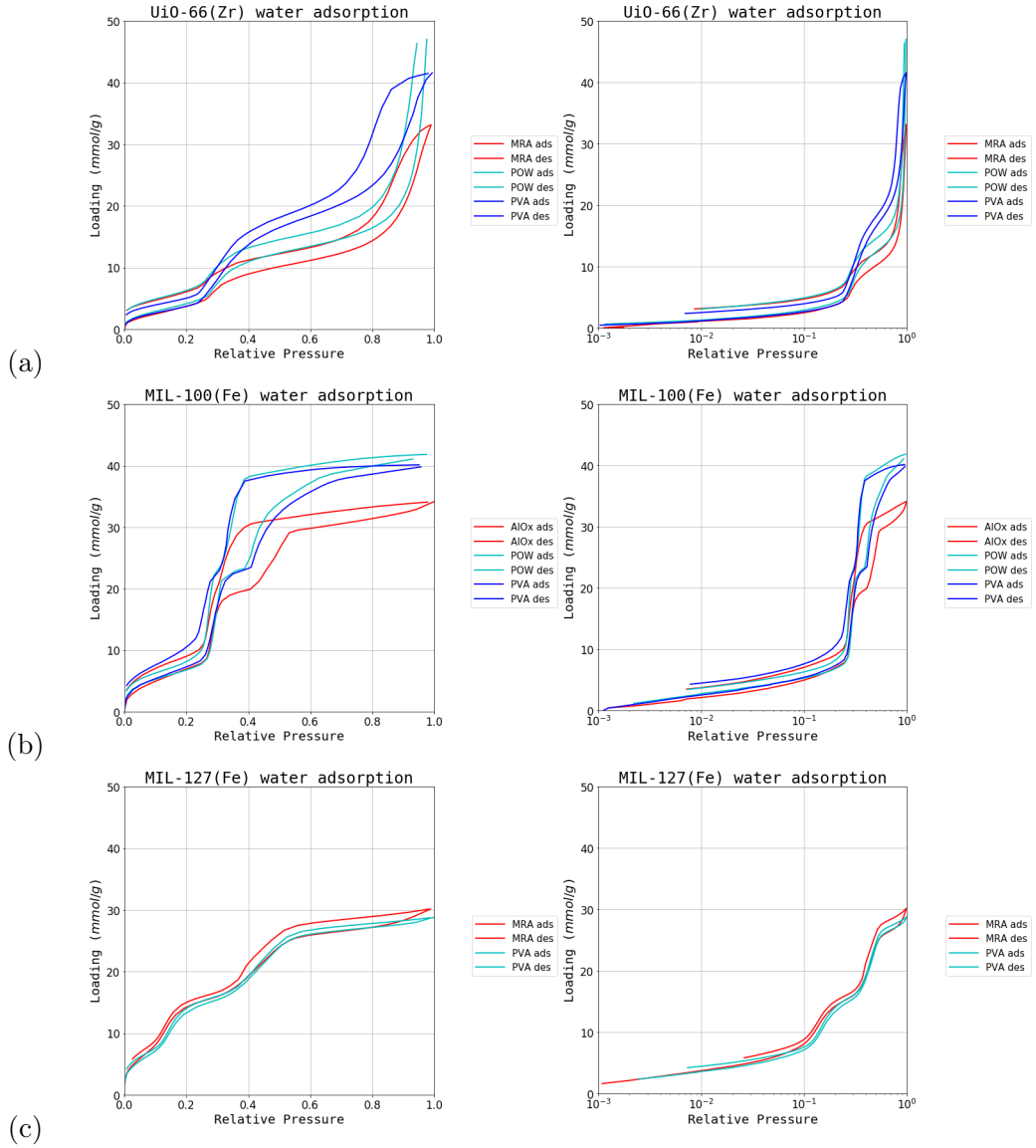


Figure 4.10: Water adsorption isotherms (a) UiO-66(Zr), (b) MIL-100(Fe) and (c) MIL-127(Fe). The powder samples are in light blue, while the  $\rho$ -alumina and poly-vinyl alcohol samples are in red and dark blue respectively. Logarithmic graphs of the isotherms are on the right for clarity of the low pressure region.

#### 4 Exploring the impact of material form on adsorption measurements

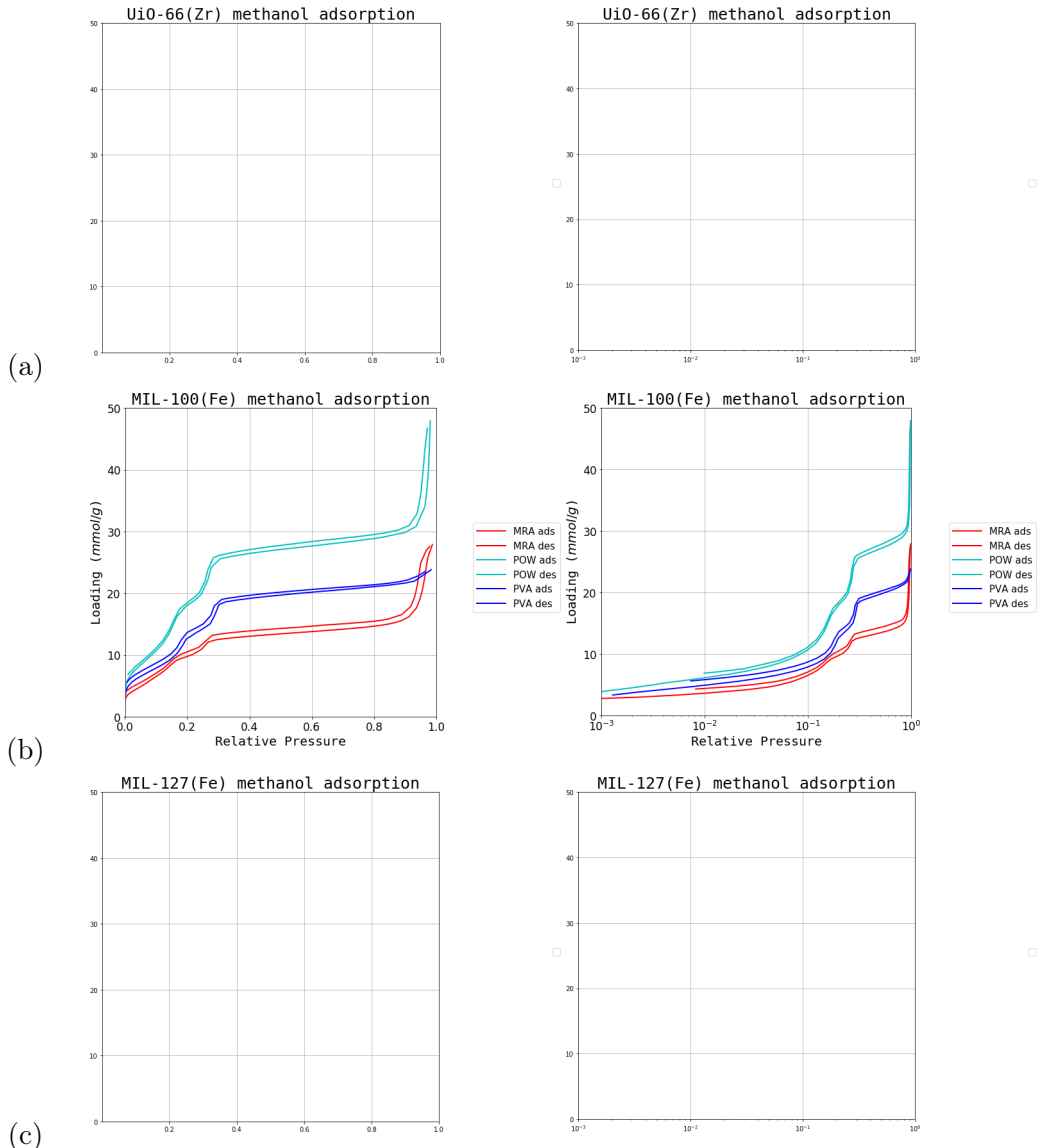


Figure 4.11: Methanol adsorption isotherms (a)  $\text{UiO-66}(\text{Zr})$ , (b)  $\text{MIL-100}(\text{Fe})$  and (c)  $\text{MIL-127}(\text{Fe})$ . The powder samples are in light blue, while the  $\rho$ -alumina and poly-vinyl alcohol samples are in red and dark blue respectively. Logarithmic graphs of the isotherms are on the right for clarity of the low pressure region.

# Bibliography

- [1] Farid Akhtar, Linnéa Andersson, Steven Ogunwumi, Niklas Hedin, and Lennart Bergström. Structuring adsorbents and catalysts by processing of porous powders. *Journal of the European Ceramic Society*, 34(7):1643–1666, July 2014. ISSN 09552219. doi: 10.1016/j.jeurceramsoc.2014.01.008.
- [2] T. Ohji, M. Singh, J. A. Salem, Dongming Zhu, and American Ceramic Society, editors. *Advanced Processing and Manufacturing Technologies for Structural and Multifunctional Materials: A Collection of Papers Presented at the 31st International Conference on Advanced Ceramics and Composites, January 21-26, 2007, Daytona Beach, Florida*. Number v. 28, issue 7 in Ceramic engineering and science proceedings. Wiley-Interscience, Hoboken, N.J, 2008. ISBN 978-0-470-19638-0. OCLC: ocn154800301.
- [3] Teresa J. Bandosz, editor. *Activated Carbon Surfaces in Environmental Remediation*. Number 7 in Interface science and technology. Elsevier/AP, Amsterdam, 2006. ISBN 978-0-12-370536-5. OCLC: 255269962.
- [4] Douglas M. Ruthven. *Principles of Adsorption and Adsorption Processes*. Wiley, New York, 1984. ISBN 978-0-471-86606-0.
- [5] Gareth T. Whiting, Abhishek Dutta Chowdhury, Ramon Oord, Pasi Paalanen, and Bert M. Weckhuysen. The curious case of zeolite–clay/binder interactions and their consequences for catalyst preparation. *Faraday Discuss.*, 188:369–386, 2016. ISSN 1359-6640, 1364-5498. doi: 10.1039/C5FD00200A.
- [6] Nina-Luisa Michels, Sharon Mitchell, and Javier Pérez-Ramírez. Effects of Binders on the Performance of Shaped Hierarchical MFI Zeolites in Methanol-to-Hydrocarbons. *ACS Catalysis*, 4(8):2409–2417, August 2014. ISSN 2155-5435, 2155-5435. doi: 10.1021/cs500353b.
- [7] Stefan Kaskel, editor. *The Chemistry of Metal-Organic Frameworks: Synthesis, Characterization, and Applications*. Wiley-VCH Verlag GmbH & Co. KGaA, Weinheim, 2016. ISBN 978-3-527-69305-4 978-3-527-33874-0 978-3-527-69308-5 978-3-527-69306-1 978-3-527-69307-8.
- [8] Enrique V. Ramos-Fernandez, Mariana Garcia-Domingos, Jana Juan-Alcañiz, Jorge Gascon, and Freek Kapteijn. MOFs meet monoliths: Hierarchical structuring metal organic framework catalysts. *Applied Catalysis A: General*, 391(1-2):261–267, January 2011. ISSN 0926860X. doi: 10.1016/j.apcata.2010.05.019.
- [9] Sonia Aguado, Jerome Canivet, and David Farrusseng. Facile shaping of an imidazolate-based MOF on ceramic beads for adsorption and catalytic applications.

## Bibliography

- Chemical Communications*, 46(42):7999, 2010. ISSN 1359-7345, 1364-548X. doi: 10.1039/c0cc02045a.
- [10] D. Bazer-Bachi, L. Assié, V. Lecocq, B. Harbuzaru, and V. Falk. Towards industrial use of metal-organic framework: Impact of shaping on the MOF properties. *Powder Technology*, 255:52–59, March 2014. ISSN 00325910. doi: 10.1016/j.powtec.2013.09.013.
  - [11] Tian Tian, Jose Velazquez-Garcia, Thomas D. Bennett, and David Fairen-Jimenez. Mechanically and chemically robust ZIF-8 monoliths with high volumetric adsorption capacity. *Journal of Materials Chemistry A*, 3(6):2999–3005, 2015. ISSN 2050-7488, 2050-7496. doi: 10.1039/C4TA05116E.
  - [12] Rocio Semino, Naseem A. Ramsahye, Aziz Ghoufi, and Guillaume Maurin. Microscopic Model of the Metal–Organic Framework/Polymer Interface: A First Step toward Understanding the Compatibility in Mixed Matrix Membranes. *ACS Applied Materials & Interfaces*, 8(1):809–819, January 2016. ISSN 1944-8244, 1944-8252. doi: 10.1021/acsami.5b10150.
  - [13] Takashi Kitao, Yuanyuan Zhang, Susumu Kitagawa, Bo Wang, and Takashi Uemura. Hybridization of MOFs and polymers. *Chemical Society Reviews*, 46(11): 3108–3133, 2017. ISSN 0306-0012. doi: 10.1039/C7CS00041C.
  - [14] Nicolas Chanut, Andrew D. Wiersum, U-Hwang Lee, Young Kyu Hwang, Florence Ragon, Hubert Chevreau, Sandrine Bourrelly, Bogdan Kuchta, Jong-San Chang, Christian Serre, and Philip L. Llewellyn. Observing the Effects of Shaping on Gas Adsorption in Metal-Organic Frameworks. *European Journal of Inorganic Chemistry*, 2016(27):4416–4423, September 2016. ISSN 14341948. doi: 10.1002/ejic.201600410.
  - [15] Jasmina Hafizovic Cavka, Søren Jakobsen, Unni Olsbye, Nathalie Guillou, Carlo Lamberti, Silvia Bordiga, and Karl Petter Lillerud. A New Zirconium Inorganic Building Brick Forming Metal Organic Frameworks with Exceptional Stability. *Journal of the American Chemical Society*, 130(42):13850–13851, October 2008. ISSN 0002-7863. doi: 10.1021/ja8057953.
  - [16] Andrew D. Wiersum, Estelle Soubeyrand-Lenoir, Qingyuan Yang, Beatrice Moulin, Vincent Guillerm, Mouna Ben Yahia, Sandrine Bourrelly, Alexandre Vimont, Stuart Miller, Christelle Vagner, Marco Daturi, Guillaume Clet, Christian Serre, Guillaume Maurin, and Philip L. Llewellyn. An Evaluation of UiO-66 for Gas-Based Applications. *Chemistry - An Asian Journal*, 6(12):3270–3280, December 2011. ISSN 18614728. doi: 10.1002/asia.201100201.
  - [17] Patricia Horcajada, Suzy Surblé, Christian Serre, Do-Young Hong, You-Kyong Seo, Jong-San Chang, Jean-Marc Grenèche, Irene Margiolaki, and Gérard Férey. Synthesis and catalytic properties of MIL-100(Fe), an iron( III ) carboxylate with large

## Bibliography

- pores. *Chem. Commun.*, (27):2820–2822, 2007. ISSN 1359-7345, 1364-548X. doi: 10.1039/B704325B.
- [18] Ji Woong Yoon, You-Kyong Seo, Young Kyu Hwang, Jong-San Chang, Hervé Leclerc, Stefan Wuttke, Philippe Bazin, Alexandre Vimont, Marco Daturi, Emily Bloch, Philip L. Llewellyn, Christian Serre, Patricia Horcajada, Jean-Marc Grenèche, Alirio E. Rodrigues, and Gérard Férey. Controlled Reducibility of a Metal-Organic Framework with Coordinatively Unsaturated Sites for Preferential Gas Sorption. *Angewandte Chemie International Edition*, 49(34):5949–5952, August 2010. ISSN 14337851. doi: 10.1002/anie.201001230.
- [19] Yunling Liu, Jarrod F. Eubank, Amy J. Cairns, Juergen Eckert, Victor Ch. Kravtsov, Ryan Luebke, and Mohamed Eddaoudi. Assembly of Metal-Organic Frameworks (MOFs) Based on Indium-Trimer Building Blocks: A Porous MOF with  $\text{soc}$  Topology and High Hydrogen Storage. *Angewandte Chemie International Edition*, 46(18):3278–3283, April 2007. ISSN 14337851, 15213773. doi: 10.1002/anie.200604306.
- [20] Hubert Chevreau, Anastasia Permyakova, Farid Nouar, Paul Fabry, Carine Livage, Florence Ragon, Alfonso Garcia-Marquez, Thomas Devic, Nathalie Steunou, Christian Serre, and Patricia Horcajada. Synthesis of the biocompatible and highly stable MIL-127(Fe): From large scale synthesis to particle size control. *CrystEngComm*, 18(22):4094–4101, 2016. ISSN 1466-8033. doi: 10.1039/C5CE01864A.
- [21] Nicolas Chanut, Sandrine Bourrelly, Bogdan Kuchta, Christian Serre, Jong-San Chang, Paul A. Wright, and Philip L. Llewellyn. Screening the Effect of Water Vapour on Gas Adsorption Performance: Application to CO<sub>2</sub> Capture from Flue Gas in Metal-Organic Frameworks. *ChemSusChem*, 10(7):1543–1553, April 2017. ISSN 18645631. doi: 10.1002/cssc.201601816.
- [22] Qingyuan Yang, Sébastien Vaesen, Florence Ragon, Andrew D. Wiersum, Dong Wu, Ana Lago, Thomas Devic, Charlotte Martineau, Francis Taulelle, Philip L. Llewellyn, Hervé Jobic, Chongli Zhong, Christian Serre, Guy De Weireld, and Guillaume Maurin. A Water Stable Metal-Organic Framework with Optimal Features for CO<sub>2</sub> Capture. *Angewandte Chemie*, 125(39):10506–10510, September 2013. ISSN 00448249. doi: 10.1002/ange.201302682.
- [23] Anil H. Valekar, Kyung-Ho Cho, U-Hwang Lee, Ji Sun Lee, Ji Woong Yoon, Young Kyu Hwang, Seung Gwan Lee, Sung June Cho, and Jong-San Chang. Shaping of porous metal-organic framework granules using mesoporous  $\rho$ -alumina as a binder. *RSC Advances*, 7(88):55767–55777, 2017. ISSN 2046-2069. doi: 10.1039/C7RA11764G.

# **5Exploring novel behaviours**

## **5.1 Introduction**



## **5.2 Literature**

## **5.3 Method**

## **5.4 Results and discussion**

## **5.5 Conclusion**

# Bibliography

# Common characterisation techniques

## 1 Thermogravimetry

TGA experiments were carried out on ca. 15 mg sample with a Q500 (TA Instruments) apparatus in a dynamic “Hi-Res” mode using  $3\text{ K min}^{-1}$  under both nitrogen and argon flow at  $30\text{ cm}^3 \text{ min}^{-1}$ . For comparison, the curves have been normalized at  $800\text{ }^\circ\text{C}$ .

## 2 Bulk density determination

Bulk density was determined by weighing 1.5 ml empty vessels and settling the powder or the spheres of the MOFs inside. Powders have been added by small increments and settled through vibration between each addition. We finally weighed the full vessels, which allowed the bulk density to be determined. The experiments were recorded with the same vessel after cleaning.

## 3 Nitrogen physisorption at 77 K

Nitrogen physisorption at 77 K was used to calculate BET areas and accessible pore volumes.<sup>(?)</sup> Approximately 60 mg of sample were used for each measurement. The adsorption experiments were carried out on a Micromeritics Triflex apparatus. The BET area on these microporous solids was calculated using the procedure devised by ? Accessible pore volume was calculated from the amount adsorbed at  $p/p^0 = 0.2$ . The pore sizes were calculated by applying the Dollimore-Heal method on the desorption branch of the isotherm.

## 4 Gravimetric isotherms measured on Rubotherm Balance

The gravimetric isotherms in this study were obtained using a commercial balance (Rubotherm GmbH). Approximately 1 g of dried sample was used for these experiments. Samples was activated in situ by heating under vacuum. The gas was introduced using a step-by-step method, and equilibrium was assumed to have been reached when the variation of weight remained below  $30\text{ }\mu\text{g}$  over a 15 min interval. The volume of the sample was determined from a blank experiment with helium as the nonadsorbing gas and used in combination with the gas density measured by the Rubotherm balance to compensate for buoyancy.

## **5 Vapour adsorption**

Adsorption of water or ethanol vapour was measured at 298 K on a BELmax apparatus (MicrotracBEL, Japan). Approximately 50 mg of material was used for each experiment.

# Synthesis method of referenced materials

## 1 UiO-66(Zr) for defect study

The Takeda 5A carbon was purchased directly from the Takeda corporation. The sample was activated at 250 °C under vacuum (5 mbar) before any measurements.

## 2 UiO-66(Zr) for defect study

The UiO-66(Zr) sample preparation was adapted from Shearer et al.<sup>(?)</sup> as follows: ZrCl<sub>4</sub> (1.55 g, 6.65 mmol), an excess of terephthalic acid (BDC) (1.68 g, 10.11 mmol), HCl 37 % solution (0.2 ml, 3.25 mmol) and N,N'-dimethylformamide (DMF) (200 ml, 2.58 mol) were added to a 250 ml pressure resistant Schott bottle. The mixture was stirred for 10 min, followed by incubation in convection oven at 130 °C for 24 h. The resulting white precipitate was washed with fresh DMF (3× 50 ml) followed by ethanol (3× 50 ml) over the course of 48 h and dried at 60 °C. After drying, the sample was activated on a vacuum oven by heating at 200 °C under vacuum for 12 h. The yield was 78 % white microcrystalline powder. Before the experiment, the sample was calcined at 250 °C under vacuum (5 mbar) to remove any residual solvents from the framework.

## 3 UiO-66(Zr) for shaping study

## 4 MIL-100(Fe) for shaping study

## 5 MIL-127(Fe) for shaping study

MIL-127(Fe) was synthesized by reaction of Fe(ClO<sub>4</sub>)<sub>3</sub> · 6 H<sub>2</sub>O (3.27 g, 9.2 mmol) and C<sub>16</sub>N<sub>2</sub>O<sub>8</sub>H<sub>6</sub> (3.3 g) in DMF (415 ml) and hydrofluoric acid (5 M, 2.7 ml) at 423 K in a Teflon flask. The obtained orange crystals were placed in DMF (100 ml) and stirred at ambient temperature for 5 h. The final product was kept at 375 K overnight. MIL-127(Fe) was synthesized by reaction of Fe(ClO<sub>4</sub>)<sub>3</sub> · 6 H<sub>2</sub>O (3.27 g, 9.2 mmol) and C<sub>16</sub>N<sub>2</sub>O<sub>8</sub>H<sub>6</sub> (3.3 g) in DMF (415 ml) and hydrofluoric acid (5 M, 2.7 ml) at 423 K in a Teflon flask. The obtained orange crystals were placed in DMF (100 ml) and stirred at ambient temperature for 5 h. The final product was kept at 375 K overnight.

# Complete adsorption dataset for shaping study

## 1 Calorimetry dataset UiO-66(Zr)

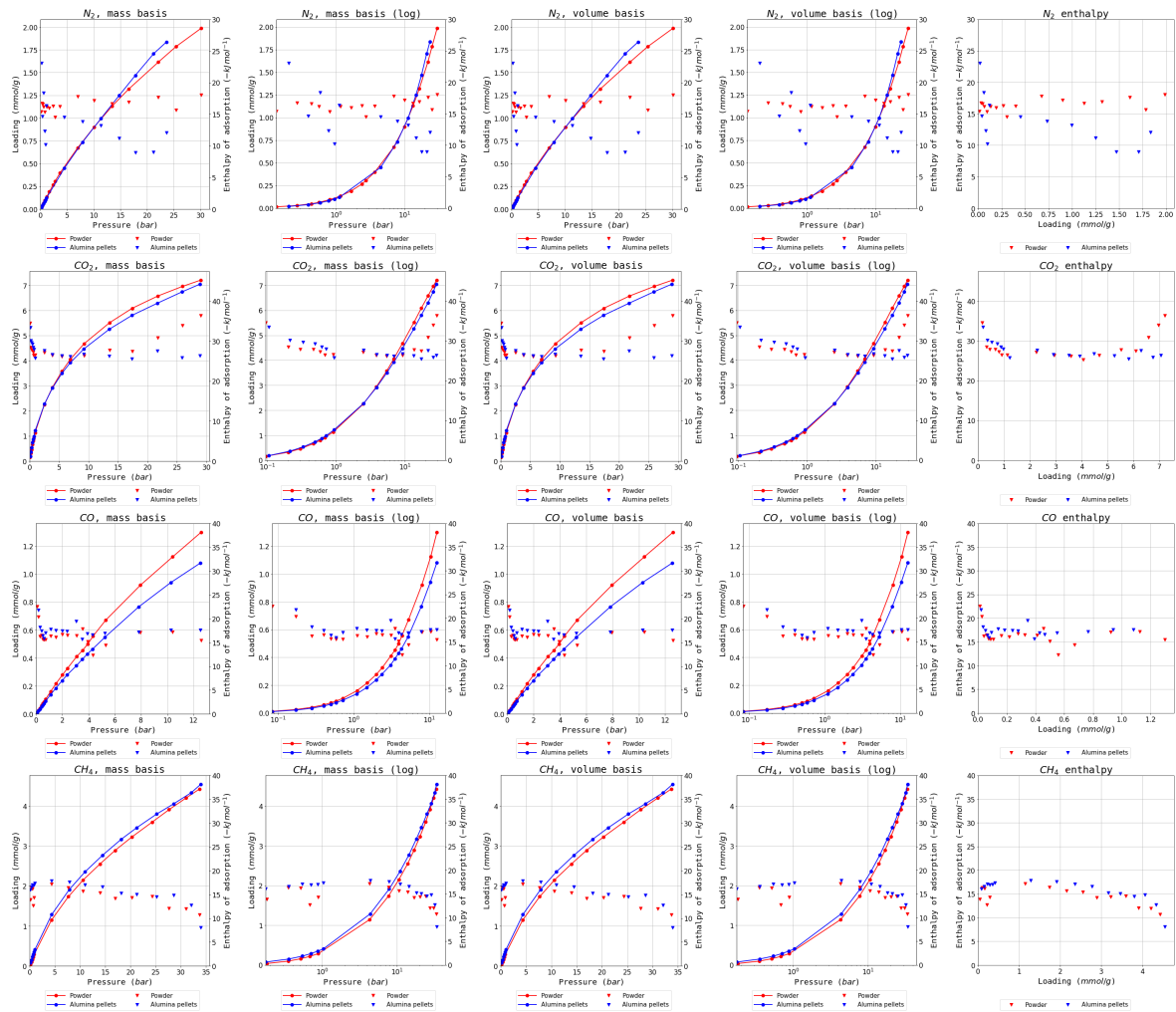


Figure 1: Complete isotherm and enthalpy dataset for UiO-66(Zr)

## Complete adsorption dataset for shaping study

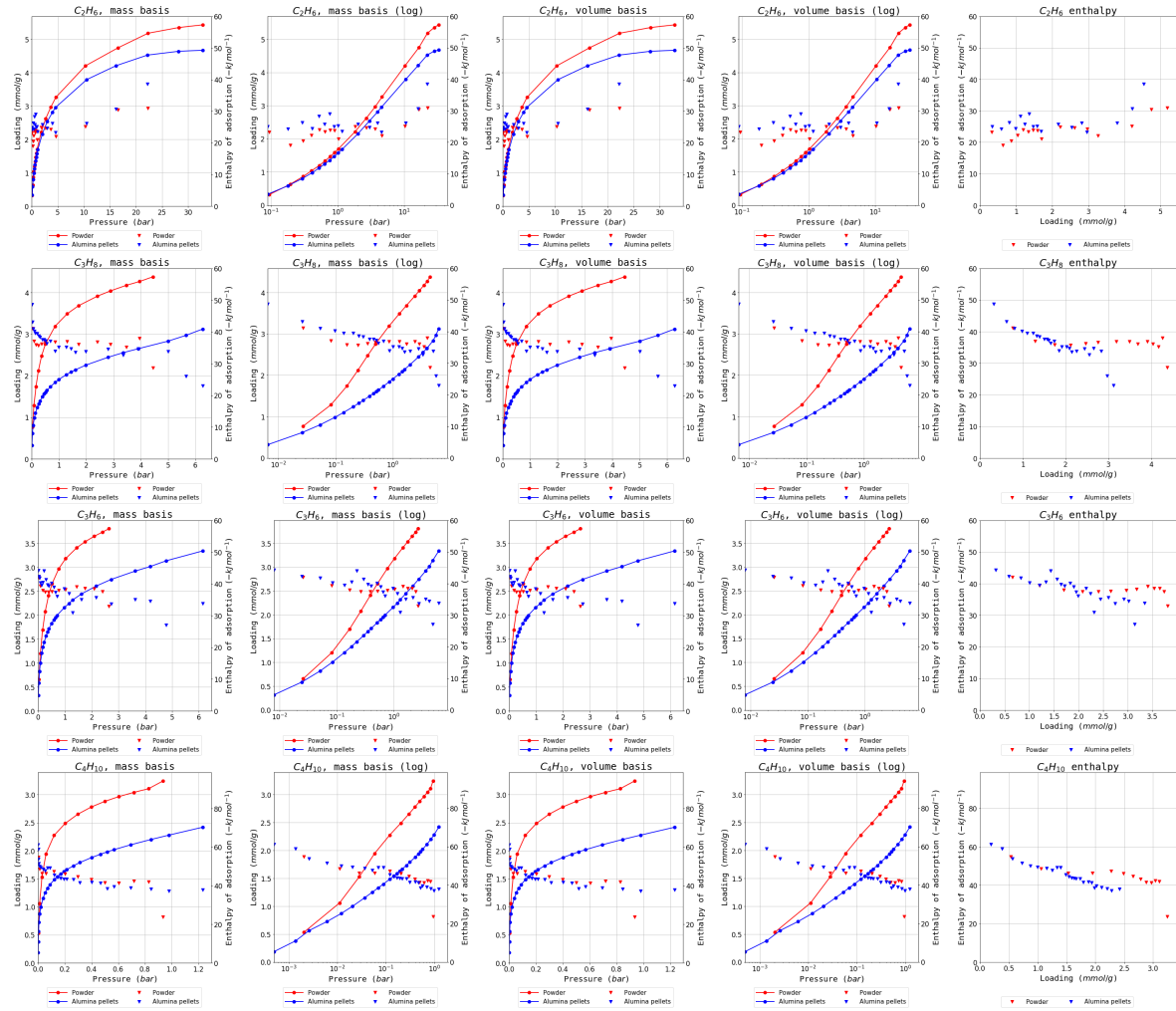


Figure 1: Complete isotherm and enthalpy dataset for UiO-66(Zr)

## 2 Calorimetry MIL-100(Fe)

## Complete adsorption dataset for shaping study

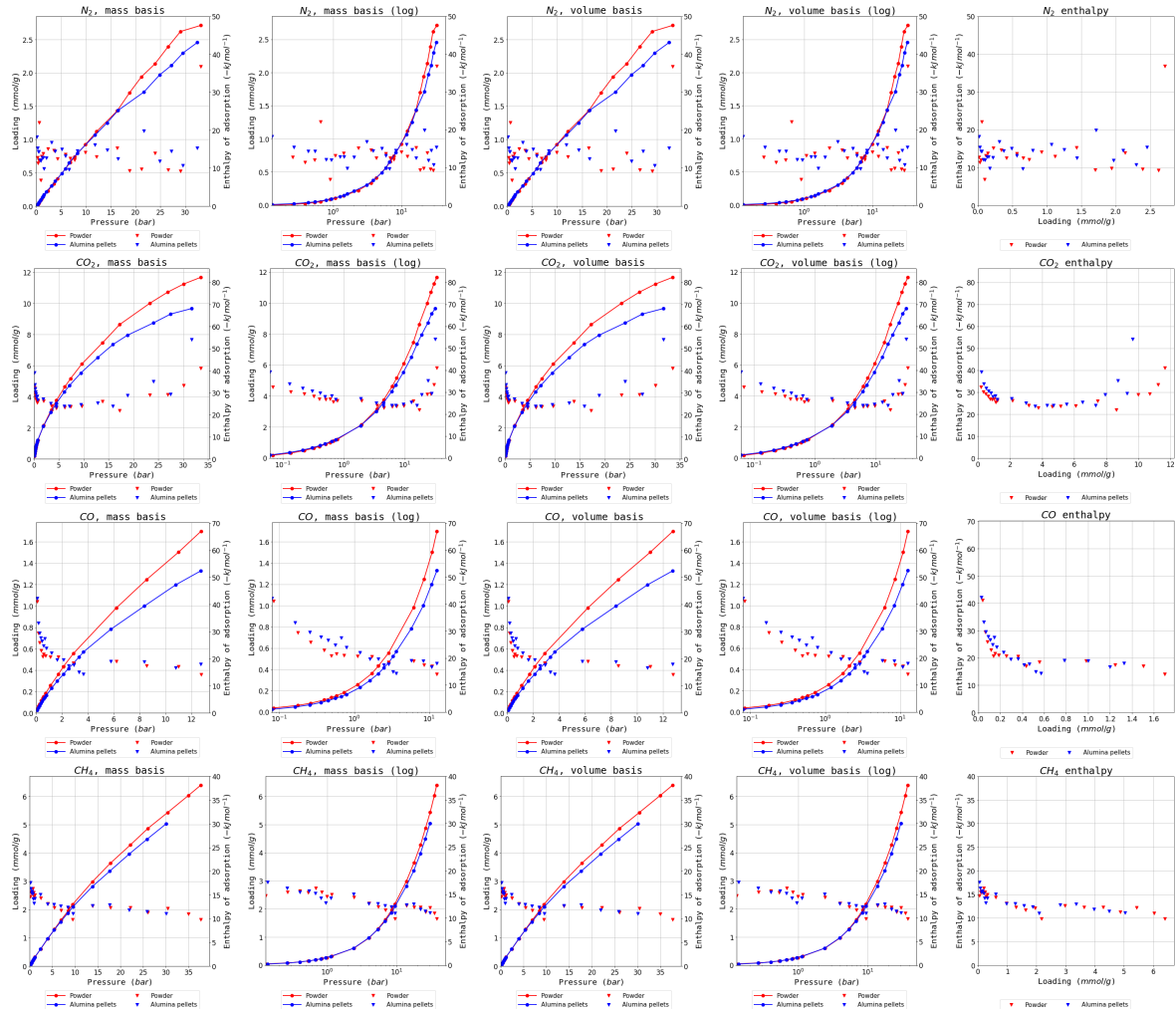


Figure 2: Complete isotherm and enthalpy dataset for MIL-100(Fe)

## Complete adsorption dataset for shaping study

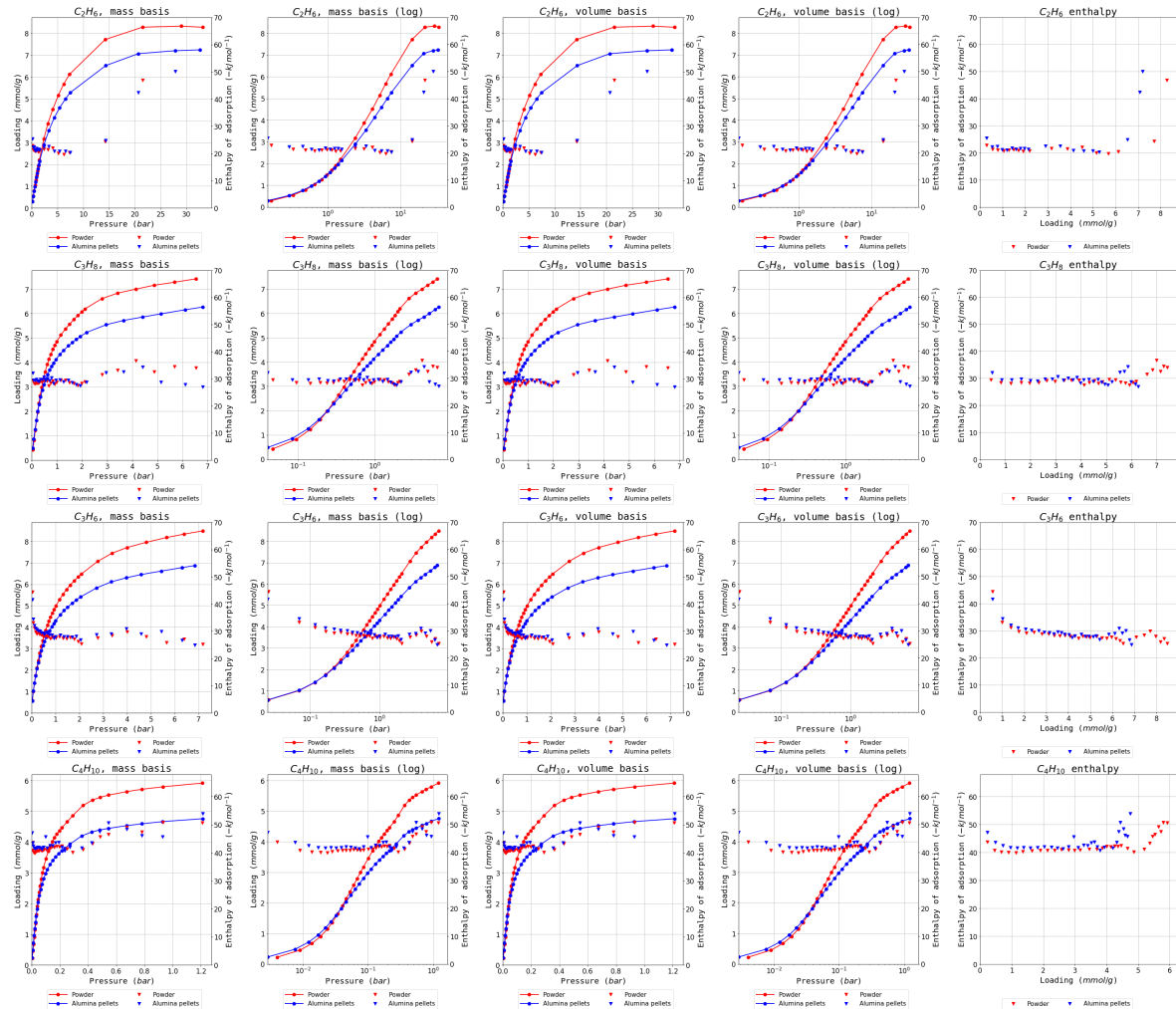


Figure 2: Complete isotherm and enthalpy dataset for MIL-100(Fe)

### 3 Calorimetry MIL-127(Fe)

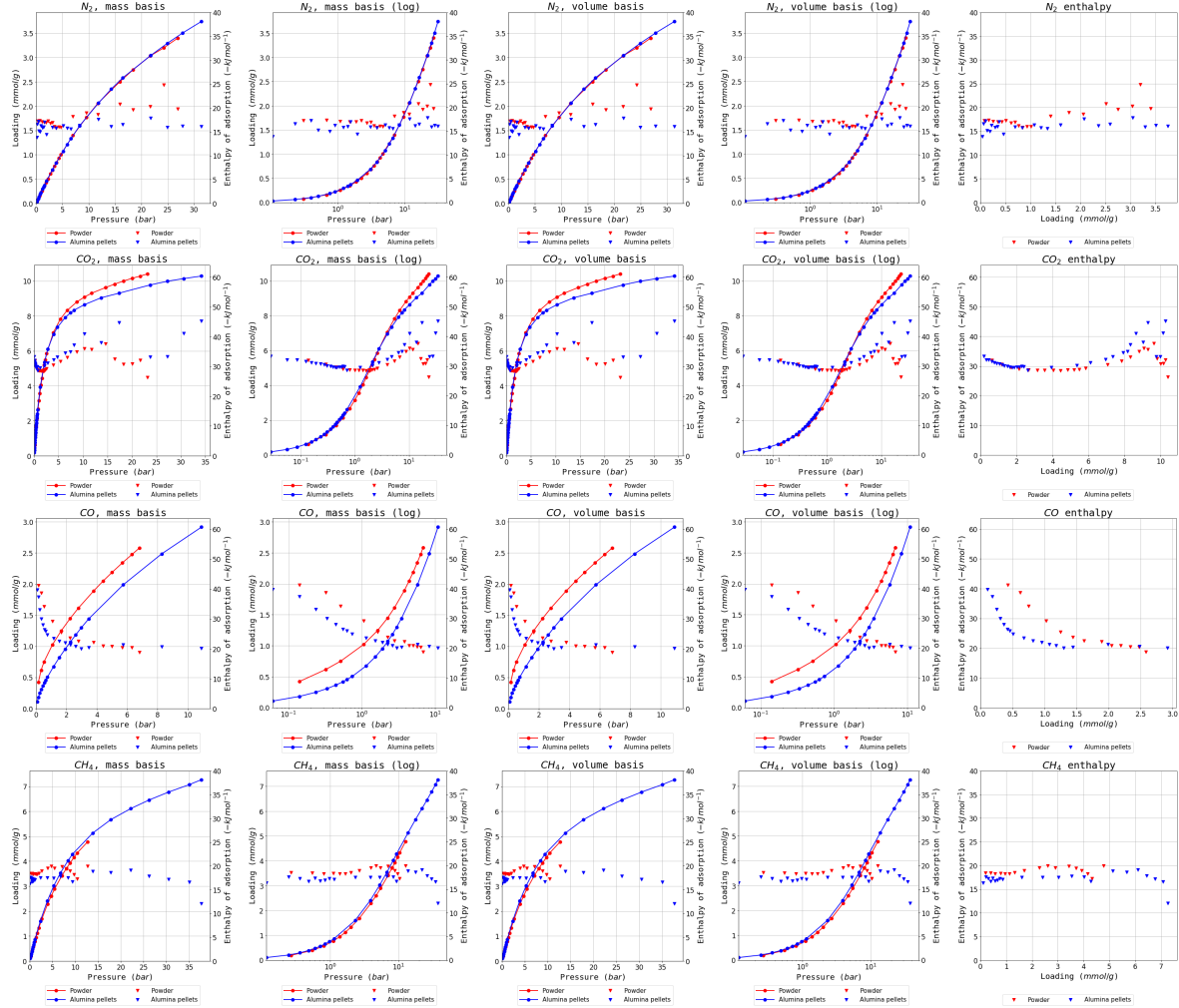


Figure 3: Complete isotherm and enthalpy dataset for MIL-127(Fe)

# Complete adsorption dataset for shaping study

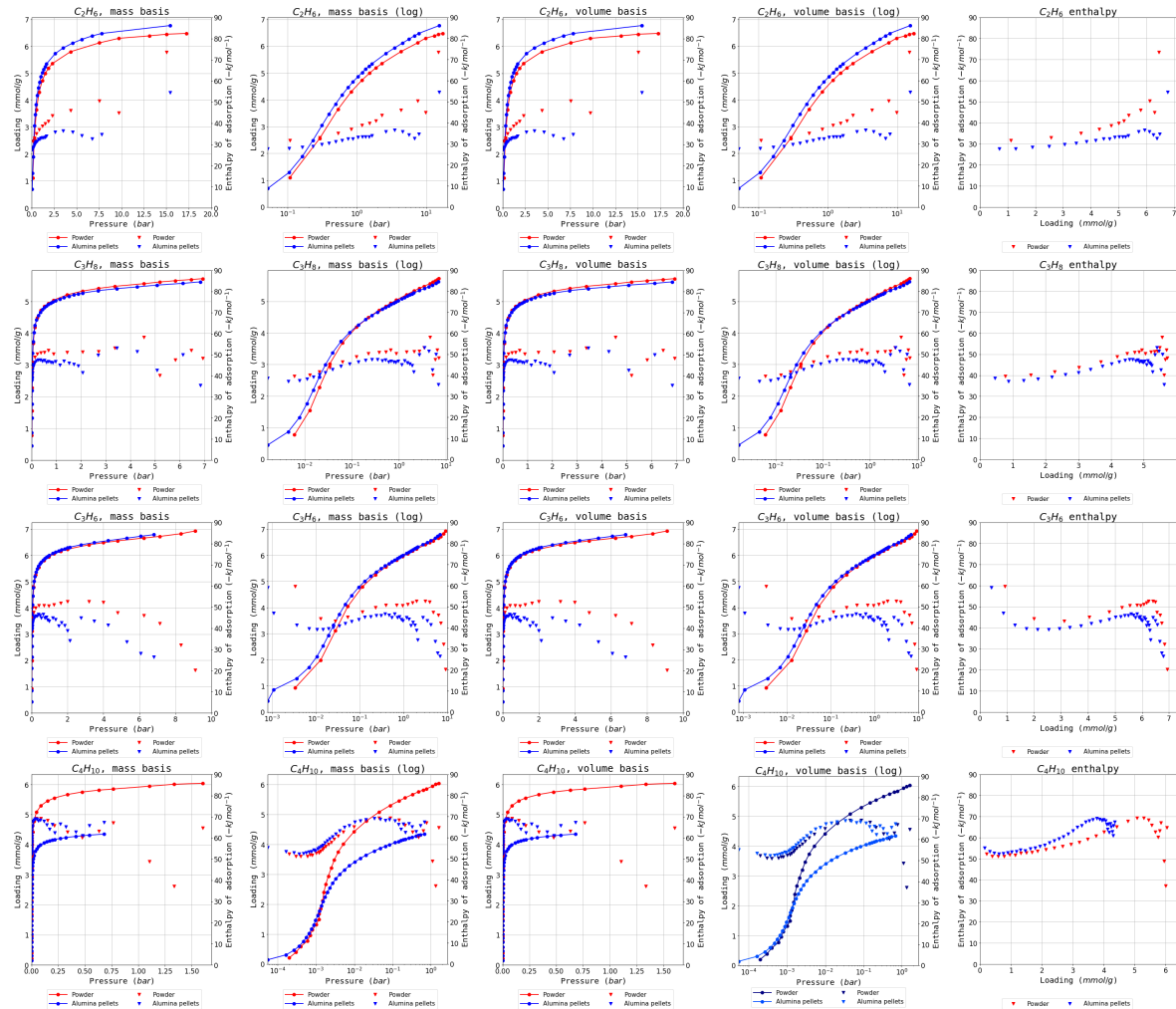


Figure 3: Complete isotherm and enthalpy dataset for MIL-127(Fe)